bioRxiv preprint doi: https://doi.org/10.1101/2023.04.26.538374; this version posted April 28, 2023. The copyright holder for this preprint (which was not certified by peer review) is the author/funder, who has granted bioRxiv a license to display the preprint in perpetuity. It is made available under aCC-BY 4.0 International license.

Mtfp1 ablation enhances mitochondrial respiration and protects against hepatic steatosis

Cecilia PATITUCCI[1*], Juan Diego HERNÁNDEZ-CAMACHO[1*], Elodie VIMONT[1], Thomas COKELAER[2,3], Thibault CHAZE[4], Quentin GIAI GIANETTO[3,4], Mariette MATONDO[3], Anastasia GAZI[5], Ivan NEMAZANYY[6], David A. STROUD[7], Daniella H. HOCK[7], Erminia DONNARUMMA[1], Timothy WAI[1**]

1- Institut Pasteur, Mitochondrial Biology Group, CNRS UMR 3691, Université Paris Cité, Paris, France.

2- Institut Pasteur, Biomics Technological Platform, Université Paris Cité, Paris, France

3- Institut Pasteur, Bioinformatics and Biostatistics Hub, Université Paris Cité, Paris, France

4- Institut Pasteur, Proteomics Core Facility, MSBio UtechS, UAR CNRS 2024, Université Paris Cité, Paris, France

5- Institut Pasteur Ultrastructural Bio Imaging, UTechS, Université Paris Cité, Paris, France.

6- Platform for Metabolic Analyses, SFR Necker, INSERM US24/CNRS UAR 3633, Paris, France.

7- Department of Biochemistry and Pharmacology, Bio21 Molecular Science and Biotechnology Institute, University of Melbourne, Victorian Clinical Genetics Services and Murdoch Children's Research Institute, Royal Children's Hospital, Melbourne, Australia

*These authors contributed equally to this work

**Correspondence: timothy.wai@pasteur.fr

Keywords : **mitochondria, liver, steatosis, NAFLD, oxidative phosphorylation**

bioRxiv preprint doi: https://doi.org/10.1101/2023.04.26.538374; this version posted April 28, 2023. The copyright holder for this preprint (which was not certified by peer review) is the author/funder, who has granted bioRxiv a license to display the preprint in perpetuity. It is made available under aCC-BY 4.0 International license.

Abstract

Hepatic steatosis is the result of an imbalance between nutrient delivery and metabolism in the liver. It is the first hallmark of Non-alcoholic fatty liver disease (NAFLD) and is characterized by the accumulation of excess lipids in the liver that can drive liver failure, inflammation, and cancer. Mitochondria control the fate and function of cells and compelling evidence implicates these multifunctional organelles in the appearance and progression of liver dysfunction, although it remains to be elucidated which specific mitochondrial functions are actually causally linked to NAFLD. Here, we identified Mitochondrial Fission Process 1 protein (MTFP1) as a key regulator of mitochondrial and metabolic activity in the liver. Deletion of *Mtfp1* in hepatocytes is physiologically benign in mice yet leads to the upregulation of oxidative phosphorylation (OXPHOS) activity and mitochondrial respiration, independently of mitochondrial biogenesis. Consequently, hepatocyte-specific knockout mice are protected against high fat diet-induced hepatic steatosis and metabolic dysregulation. Additionally, we find that deletion of *Mtfp1* in liver mitochondria inhibits mitochondrial permeability transition pore opening in hepatocytes, conferring protection against apoptotic liver damage in vivo and ex vivo. Our work uncovers novel functions of MTFP1 in the liver, positioning this gene as an unexpected regulator of OXPHOS and a therapeutic candidate for NAFLD.

bioRxiv preprint doi: https://doi.org/10.1101/2023.04.26.538374; this version posted April 28, 2023. The copyright holder for this preprint (which was not certified by peer review) is the author/funder, who has granted bioRxiv a license to display the preprint in perpetuity. It is made available under aCC-BY 4.0 International license.

Introduction

Non-alcoholic fatty liver disease (NAFLD) is the most common chronic liver disease in industrialized countries, whose incidence is rapidly expanding worldwide[1]. NAFLD is a frequent comorbidity of type 2 diabetes and obesity with its prevalence calculated at ~30% in the general population and 80% among obese people. NAFLD encompasses a spectrum of pathologies ranging from simple steatosis characterized by triglyceride accumulation in hepatocytes, to non-alcoholic steatohepatitis (NASH), whose hallmarks are inflammation and fibrogenesis, which can further progress into cirrhosis and hepato-cellular carcinoma (HCC), the deadliest form of liver cancer[2].

Considerable efforts have been made in recent decades to better understand the mechanisms of NAFLD progression and therapeutic targets that might subsequently alleviate the burden of this spectrum of pathologies. The progression of NAFLD is currently explained by a "multiple parallel-hit" hypothesis, which implicates the synergistic and concerted action of multiple events originating from various liver cell types[3]. In hepatocytes, oxidative stress and mitochondrial dysfunction have been suggested to contribute to hepatocyte damage and death, tissue inflammation and fibrosis[4]. This model highlights the complexity and heterogeneity of NAFLD progression and underscores the central involvement of hepatocytes mitochondria in the progression of NAFLD. Mitochondria are essential organelles that are deeply integrated in cellular homeostasis. Most famous for their production of ATP via oxidative phosphorylation (OXPHOS), mitochondria also regulate programmed cell death and inflammation through the sequestration and release of pro-apoptotic factors and pro-inflammatory molecules[5,6]. Yet which of the multiple functions of mitochondria are directly implicated in the onset of steatosis, inflammation, hepatocyte death, and subsequent tissue remodeling has not been defined[7].

The relevance of mitochondria to liver function is highlighted by mitochondrial dysfunction observed in inborn and acquired liver pathologies: mutations in mitochondrial genes that cause genetic diseases manifest with liver dysfunction, while strong associations also exist between mitochondrial dysfunction and acquired liver diseases such as NAFLD, viral hepatitis, and ischemic liver injury[8,9]. Mitochondrial respiration has been reported to decline during the progression of liver dysfunction in humans[10] and perturbation of mitochondrial structure has been reported in liver

bioRxiv preprint doi: https://doi.org/10.1101/2023.04.26.538374; this version posted April 28, 2023. The copyright holder for this preprint (which was not certified by peer review) is the author/funder, who has granted bioRxiv a license to display the preprint in perpetuity. It is made available under aCC-BY 4.0 International license.

biopsies from patients with NASH[11], lending support to the notion that the maintenance of mitochondrial integrity is paramount to liver function. Promoting enhanced oxygen consumption with targeted uncouplers in the liver reduces the deleterious accumulation of hepatic lipid storage and steatosis in rodents and primates[12,13], yet broader system-wide mitochondrial uncoupling has catastrophic effects on other organs and is incompatible with life[14]. We recently showed that mitochondrial uncoupling in cardiac mitochondria is regulated by Mitochondrial Fission Process 1 (MTFP1), uncovering a novel role of this protein in bioenergetic regulation[15]. MTFP1 is a protein localized at the inner membrane (IMM) whose namesake derives from a putative role in mitochondrial fission in vitro[16,17] and has garnered interest as marker of liver dysfunction in humans. Retrospective studies revealed a link between *MTFP1* expression in tumoral tissue and patient survival in HCC[18], the most common type of liver cancer, whose development is heavily influenced by NAFLD progression[2]. Indeed, compelling evidence implicates MTFP1 in metabolic sensing and programmed cell death regulation in vitro[17,19,20], although its pertinence in the liver function and metabolism has never been explored.

Here, we report the generation of a liver-specific *Mtfp1* knockout mouse model (LMKO) and discover that, contrary to what we observed for the heart[15], MTFP1 is dispensable for organ function. We report that deletion of *Mtfp1* in vivo in hepatocytes enhances hepatic OXPHOS activity and confers protection against diet-induced liver steatosis, weight gain and systemic glucose dysregulation when mice are fed a high fat diet (HFD). In sum, our data reveal liver-specific effects of MTFP1 ablation in vivo that position this gene as a therapeutic candidate for NAFLD.

bioRxiv preprint doi: https://doi.org/10.1101/2023.04.26.538374; this version posted April 28, 2023. The copyright holder for this preprint (which was not certified by peer review) is the author/funder, who has granted bioRxiv a license to display the preprint in perpetuity. It is made available under aCC-BY 4.0 International license.

Results

Generation and characterization of liver specific *Mtfp1* KO mouse model

To investigate the link between mitochondrial function and liver metabolism we generated a liver-specific KO mouse model in which we specifically deleted *Mtfp1* in post-natal hepatocytes (LMKO mice; Fig. 1A, S1A-B). Conditional mice ($Mtfp1^{LoxP/LoxP}$) previously generated on a C57Bl6/N background[15] were crossed to Alb-Cre recombinase transgenic mice ($Alb\text{-}Cre^{tg/+}$) to generate LMKO mice ($Alb\text{-}Cre^{tg/+}Mtfp1^{LoxP/LoxP}$). Genetic deletion of *Mtfp1* in LMKO mice was specific to the liver (Fig. 1B) and caused a profound depletion of mRNA (Fig. 1C) and protein (Fig. 1D) expression in liver extracts. MTFP1 ablation in hepatocytes did not affect perinatal survival (Fig. 1E) and histological liver analysis performed on LMKO mice were unremarkable and indistinguishable from those of control littermates (Fig. 1F). Contrary to the ablation of MTFP1 in the heart[15], LMKO mice did not manifest any overt defects during their lifetime under normal chow diet (NCD). Comprehensive assessment of liver structure and function revealed no defects: liver mass (Fig. 1G) was unchanged in LMKO mice and the levels of circulating biomarkers of liver damage such as alanine aminotransaminase (ALAT) and aspartate aminotransaminase (ASAT) were not increased relative to those of control littermates (Fig. 1H). Circulating levels of cholesterol and triglycerides were normal (Fig. 1I) and metabolic cage performance was not impaired (Fig. 1J-S1C). Similarly, we observed no evidence of pathological gene expression changes by RNAseq analysis (Fig. S1D, Supplemental Dataset 1). In fact, control and LMKO livers revealed virtually no gene dysregulation (only 27 out of >25,000 transcripts) including no upregulation of established markers[21] of NAFLD or HCC defined in humans (Fig. S1D, Supplemental Dataset 1). Taken together, our observations demonstrate that the deletion of *Mtfp1* in hepatocytes does not negatively impact the liver under basal conditions.

Mtfp1 deletion increases OXPHOS activity and mitochondrial respiration

Given our previous observations that MTFP1 ablation reduces bioenergetic efficiency of cardiac mitochondria[15], we decided to directly assess the impact of *Mtfp1* deletion on hepatic mitochondrial bioenergetics. To this end, we performed high resolution fluor-respirometry on isolated hepatic mitochondria isolated from control and LMKO mice, simultaneously measuring

bioRxiv preprint doi: https://doi.org/10.1101/2023.04.26.538374; this version posted April 28, 2023. The copyright holder for this preprint (which was not certified by peer review) is the author/funder, who has granted bioRxiv a license to display the preprint in perpetuity. It is made available under aCC-BY 4.0 International license.

both oxygen consumption rates (JO_2) and mitochondrial membrane potential ($\Delta\Psi$) changes with Rhodamine 123 (RH-123)[22]. JO_2 and RH-123 were recorded from mitochondria incubated with respiratory substrates promoting the delivery of electrons to complex I (state 2; pyruvate, glutamate, and malate (PGM) or complex II (state 2; succinate and rotenone), and also in the presence of palmitoyl-carnitine plus malate then in the phosphorylating (state 3: ADP), non-phosphorylating (state 4: oligomycin (OLGM) to inhibit ATP synthase) (Fig. 2A). Notably, and in contrast to MTFP1-deficient cardiac mitochondria[15], respiration in LMKO liver mitochondria was significantly increased in phosphorylating (state 3) conditions in the presence of any of the respiratory substrates we tested. Pyruvate, glutamate, and malate led to a 49% increase in state 3 respiration and succinate and rotenone led to a 57% increase in respiration (Fig. 2B). Interestingly, we observed a 200% increase in state 3 respiration in the presence of palmitoyl carnitine, a fatty acid ester derivative, pointing to an increased efficiency of fatty-acid derived energy metabolism caused by hepatocyte-specific deletion of *Mtfp1*.

Additionally, LMKO liver mitochondria showed a higher respiratory control ratio (RCR) in the presence palmitoyl carnitine plus malate (Fig 2C). Despite a marked increase in state 3 respiration, we did not observe a genotype-specific difference in mitochondrial membrane potential (Fig. 2D), which initially surprised us since increased oxygen consumption rates are typically accompanied by reduction in membrane potential due to dissipation of the protonmotive force via complex V (to synthesize ATP). The most parsimonious explanation for this result is that MTFP1 ablation promotes a commensurate increase in the activities of both cytochrome *c* oxidase (complex IV) and the ATP synthase (complex V). Indeed, when we measured the specific activities of complex IV (Fig. 2E) and complex V (Fig. 2F) in separate assays, we found a ~20% increase in LMKO mitochondria relative to control littermate controls, suggesting a similar contribution of both complexes to increase respiration while maintaining mitochondrial membrane potential. We further confirmed our findings by measuring oxygen consumption rates in mitoplasts supplied with either NADH, Cyt c, succinate and rotenone to drive electron transport via Complex II or NADH, Cyt c, succinate and malonate to drive electron transport via Complex I (Fig. 2G). In both assays, oxygen consumption was elevated in LMKO liver mitochondria demonstrating that Complex IV activity is intrinsically augmented upon MTFP1 ablation independently of the protonmotive force. Together,

bioRxiv preprint doi: https://doi.org/10.1101/2023.04.26.538374; this version posted April 28, 2023. The copyright holder for this preprint (which was not certified by peer review) is the author/funder, who has granted bioRxiv a license to display the preprint in perpetuity. It is made available under aCC-BY 4.0 International license.

these observations implied either that MTFP1 ablation triggers a specific upregulation of components of the OXPHOS machinery or the induction of a general mitochondrial biogenesis response. To differentiate between these possibilities, we assessed mitochondrial mass using multiple molecular and imaging-based methods. Quantification of mitochondrial mass in primary hepatocytes isolated from control or LMKO mice expressing a genetically encoded matrix-targeted YFP (mitoYFP) showed no differences in fluorescent signal intensity or surface area (Fig. S2A B), indicating that mitochondrial mass is unaffected by MTFP1 ablation in primary hepatocytes. Interestingly, we found a modest increase in mitochondrial elongation in LMKO mitochondria (Fig. S2C) quantified by supervised machine learning[23], consistent with previous studies in cultured cells[15,17]. Quantification of mtDNA content in liver tissue revealed no genotype-specific differences in mice fed a NCD (Fig. S2D) and transmission electron microscopy (TEM) analyses of liver sections showed no differences in mitochondrial area between control and LMKO mice (Fig. S2E). RNAseq analyses showed no evidence of gene expression signatures typically associated with increased mitochondrial biogenesis or integrated stress responses (Fig. S2E, Supplemental Dataset 1) and shotgun liver proteomics performed on control and LMKO liver extracts revealed no global upregulation of mitochondrial proteins (Fig. 1D, Supplemental Dataset 2). Taken together, our data strongly argue that a specific and coordinated increase in both complex IV and V activity in hepatocytes enhances respiration in liver mitochondria deleted of *Mtfp1,* enabling them to consume nutrient-derived respiratory substrates at an elevated rate.

MTFP1 interacts with OXPHOS-related proteins in the liver.

To gain insights into the mechanisms responsible for the increased specific activities, we assessed the relative complex abundance by grouping mitochondrial proteins quantified by proteomics in the liver of NCD-fed LMKO mice according to the macromolecular complexes to which they belong (Fig. 2H, Supplemental Dataset 2). These data revealed a significant increase in Complex V subunits, which could be confirmed by quantitative SDS-PAGE (Fig. 2I) and Blue-native polyacrylamide gel electrophoresis (BN-PAGE) analyses (Fig. 2J). BN-PAGE analysis of the steady-state levels of OXPHOS complexes in LMKO liver mitochondria revealed an increase in Complex V dimers (Fig. 2J) to an increase commensurate with the reported increase in ATPase

bioRxiv preprint doi: https://doi.org/10.1101/2023.04.26.538374; this version posted April 28, 2023. The copyright holder for this preprint (which was not certified by peer review) is the author/funder, who has granted bioRxiv a license to display the preprint in perpetuity. It is made available under aCC-BY 4.0 International license.

activity (Fig. 2F). Taken together, our data suggest that improved assembly and/or maintenance of Complex V along with an increased activity of Complex IV is responsible for the enhanced respiration observed in LMKO liver mitochondria.

To gain insights into the relationship between MTFP1 and macromolecular complex assembly in the inner mitochondrial membrane (IMM), we sought to assess the interactome of MTFP1 in the liver. We generated a hepatocyte-specific transgenic mouse model enabling the expression of FLAG-MTFP1 from the *Rosa26* locus (Fig. 3A). We verified that the Hepatocyte$^{FLAG\text{-}MTFP1}$ mice, expressed FLAG-MTFP1 correctly in the IMM by protease protection assay (Fig. 3B). We then subjected liver mitochondria to co-immunoprecipitation (co-IP) and mass spectrometry (MS/MS) to define interacting protein partners, which enabled the identification of 112 specific interactors of MTFP1 with fold change (FC) >2 by MS/MS analysis (Figure 3C, D, Supplemental Dataset 3) that could be ascribed to the mitochondrial proteome according to the Mitocarta 3.0 compendium[24]. We then decided to subdivide this list into binary and enriched interactors: binary interactors were those proteins we could only identify in Hepatocyte$^{FLAG\text{-}MTFP1}$ but not control liver mitochondria CoIP eluates while enriched interactors were those proteins for which peptide abundance was greater in CoIP eluates from Hepatocyte$^{FLAG\text{-}MTFP1}$ mice than in control mice.

Classification of binary interacting proteins revealed a wide range of mitochondrial functions, with a conspicuous abundance of factors involved in mitochondrial translation and OXPHOS (Fig. 3D). On the other hand, enriched interactors did not reveal an enrichment of proteins required for mitochondrial translation, but rather those involved in various metabolic processes within mitochondria, including carrier proteins of the SLC25A family. 2D-BN-PAGE analyses revealed the formation of an MTFP1 macromolecular complex in liver mitochondria, which was absent in LMKO mice, and that co-migrated with SLC25A4 (ANT1) (Fig. 3E), as we recently described in the heart[15]. However, we found little overlap with the cardiac interactome of MTFP1[15] (7 out of 113 proteins), implying that there may be tissue-specific physical interactions and complex assembly associated with MTFP1 beyond ANT1 that regulate respiration. Altogether, these data indicate that post-transcriptional modulation of mitochondrial gene expression and IMM complex abundance and activities are induced in a specific manner by the deletion of MTFP1 in hepatocytes, leading to enhanced mitochondrial respiration.

bioRxiv preprint doi: https://doi.org/10.1101/2023.04.26.538374; this version posted April 28, 2023. The copyright holder for this preprint (which was not certified by peer review) is the author/funder, who has granted bioRxiv a license to display the preprint in perpetuity. It is made available under aCC-BY 4.0 International license.

213

214 **_Mtfp1_ deletion protects against hepatic steatosis induced by high fat diet**

215 Given enhanced stimulated respiratory activity of LMKO liver mitochondria, we next
216 decided to assess the response of LMKO mice to high fat diet (HFD) feeding, a classical metabolic
217 burden for the liver that causes nutrient overload, hepatic steatosis, and systemic metabolic
218 dysregulation that can be counteracted by accelerating oxygen consumption via mitochondrial
219 uncoupling[12,13]. We fed control and LMKO mice a HFD for a period of 16 weeks beginning at 8
220 weeks of age, which was previously shown to drive diet-induced obesity and NAFLD[25]. In control
221 mice, we observed that chronic HFD feeding triggered the hypertrophy of livers (Fig. 4A), which
222 were appreciably paler and heavier (Fig. 4B) than those of control mice on NCD. HFD feeding
223 also induced weight gain (Fig. 4C) and accumulation of hepatic triglycerides (TG), (Fig. 4D).
224 Histological analyses showed a massive accumulation of lipid droplets (in white), consistent with
225 both micro- and macro-steatosis (Fig. 4E). In contrast, HFD-fed LMKO mice were protected from
226 weight gain (Fig. 4C) and liver dysfunction, exhibiting a 26% of reduction in liver mass compared to
227 diet-matched controls (Fig. 4A, 4B). Concordantly, histological analyses of livers from HFD-fed
228 LMKO mice revealed a reduction in steatosis (Fig. 4E), a complete rescue of hepatic triglycerides
229 accumulation back to levels measured in NCD-treated mice (Fig. 4D), and a reduction in circulating
230 levels of ALAT by 64% and ASAT by 32% (Fig. 4F). Metabolic protection against HFD-feeding in
231 LMKO mice was reflected at the molecular level: liver RNAseq analyses showed that HFD feeding
232 induced significant transcriptional dysregulation in control livers with 854 upregulated genes and
233 758 downregulated genes (Fig. 4G, S3). Gene ontology analyses revealed an enrichment of
234 various metabolic pathways dysregulated by HFD-feeding in control mice including, lipid and
235 branched chain amino acid metabolism, PPAR signaling, and steroid biosynthesis, and fatty acid
236 metabolism. These alterations were absent in HFD-fed LMKO mice, in which only 214 upregulated
237 genes and 164 downregulated genes were detected, most of which were involved in pathways of
238 stress response and immune signaling (Fig. 4H). At the protein level, we observed that in HFD
239 feeding in control mice induced global reduction in complex IV by liver proteomic analyses (Fig.
240 S4A). This response was blunted in LMKO mice (Fig. S4B), leading to a relative increase in

bioRxiv preprint doi: https://doi.org/10.1101/2023.04.26.538374; this version posted April 28, 2023. The copyright holder for this preprint (which was not certified by peer review) is the author/funder, who has granted bioRxiv a license to display the preprint in perpetuity. It is made available under aCC-BY 4.0 International license.

complex IV proteins in HFD-fed LMKO mice compared to littermate, diet-matched controls (Fig. S4C).

Given the protection against hepatocyte and liver damage observed in vivo and in vitro upon the deletion of *Mtfp1*, we asked whether the protection against HFD-induced metabolic dysregulation of the liver could be explained by differential sensitivity to cell death. However, TUNEL assays performed on histological sections from HFD-fed control and LMKO mice revealed an absence hepatocyte apoptosis (Fig. 4I), which is consistent with previous findings that HFD causes limited liver cell death[25]. Altogether, our data demonstrate that *Mtfp1* deletion in hepatocytes confers metabolic resistance to hepatic steatosis in vivo (Fig. 4J) in a manner that is independent of apoptotic resistance.

Mtfp1 deletion improves hepatocyte metabolism in a cell-autonomous.

Having demonstrated that LMKO mice are protected against diet-induced steatosis, we next sought to define the breadth of systemic protection by performing a battery of metabolic tests on control and LMKO mice after HFD-feeding. Fat accumulation is known to affect systemic glucose homeostasis. Consistent with improved liver metabolism promoted by the ablation of MTFP1 in hepatocytes, metabolic cage analyses revealed improved systemic respiration in LMKO mice fed an HFD. The lower respiratory exchange ratio (RER) observed in LMKO mice (Fig. 5A) suggests that LMKO mice metabolize nutrient-derived lipids more efficiently than control littermates, which can very likely be attributed to intrinsic differences in the livers of these mice. Food and water intake were not altered between control and LMKO mice nor were distance measurement on HFD (Fig. S5A-C), pointing to a specific effect of MTFP1 on energy expenditure by the liver that is revealed under HFD feeding. Metabolic dysregulation caused by HFD feeding is known to increase *de novo* glucose synthesis by the liver of rodents[27] and so we sought to assess gluconeogenesis by performing intraperitoneal pyruvate tolerance tests (IP-PTT). We observed a 1.5-fold increase blood glucose levels in HFD-fed control mice relative to NCD littermates, which was reduced by 14% in the HFD-fed LMKO group (Fig. 5B), indicating that *Mtfp1* deletion in hepatocytes protects the liver against diet-induced dysregulation of gluconeogenesis. Consistent with these findings, intraperitoneal glucose tolerance tests (IP-GTT) revealed LMKO mice to be

bioRxiv preprint doi: https://doi.org/10.1101/2023.04.26.538374; this version posted April 28, 2023. The copyright holder for this preprint (which was not certified by peer review) is the author/funder, who has granted bioRxiv a license to display the preprint in perpetuity. It is made available under aCC-BY 4.0 International license.

modestly protected from HFD-induced glucose intolerance. In control mice, HFD feeding led to a 1.7-fold increase of the area under curve (AUC) of IP-GTT relative to normal chow diet (NCD) controls, which reduced by 17% in HFD-fed LMKO mice relative to diet-matched controls (Fig. 5C). To exclude that improved glucose tolerance in HFD-fed LMKO mice was the consequence of altered insulin resistance, rather than improved gluconeogenesis, we performed intraperitoneal insulin tolerance tests (IP-ITT). We observed no genotype-specific differences in insulin sensitivity (Fig. 5D) on either HFD or NCD, indicating that improved glucose tolerance in LMKO mice is not caused by increased systemic insulin sensitivity. Concordantly, we did not observe differences in basal insulin levels between control and LMKO mice fed a NCD (Fig S5E). While LMKO mice gained less weight upon HFD feeding (Fig. 4C), we observed no genotype-specific differences in body mass composition by NMR minispec analysis (Fig. 5E) nor in the circulating levels of cholesterol and triglycerides (Fig. 4F). In line with these findings, LMKO mice were not protected from extra-hepatic fat mass accumulation (Fig. 5G), white adipose tissue accumulation nor adipocyte hypertrophy (Fig. S5E, F), all of which are common metabolic consequences of diet-induced obesity[17,19,28]. Altogether, our data demonstrate that the protection against diet-induced metabolic dysregulation conferred to mice by hepatocyte-specific deletion of *Mtfp1* is primarily restricted to the liver.

To determine whether hepatocyte deletion of *Mtfp1* prevents steatosis in a cell-autonomous manner, we established an assay in which we could mimic HFD-induced steatosis in primary hepatocytes isolated from NCD-fed mice. Primary hepatocytes were plated and cultured in the presence of Intralipid (IntLip): a complex lipid emulsion composed of linoleic, oleic, palmitic, and stearic acids, which are the most abundant fatty acids found in HFD. We optimized our assay conditions to ensure that limited damage, death, or differentiation under both treated and non-treated (NT) conditions was occurring. Indeed, IntLip feeding of primary hepatocytes isolated from NCD-fed control mice led to a 1.6-fold increase in intracellular lipid accumulation after 24 hours, which could be visualized by live-cell imaging with BODIPY fluorescence (Fig. 5H) and quantified by high-throughput confocal imaging (Figure 5I). Notably, deletion of *Mtfp1* in primary hepatocytes rescued this phenotype: BODIPY staining intensities in NT and IntLip-treated *Mtfp1*$^{-/-}$ cells were indistinguishable to those of NT primary hepatocytes isolated from control littermates. Thus, we

bioRxiv preprint doi: https://doi.org/10.1101/2023.04.26.538374; this version posted April 28, 2023. The copyright holder for this preprint (which was not certified by peer review) is the author/funder, who has granted bioRxiv a license to display the preprint in perpetuity. It is made available under aCC-BY 4.0 International license.

conclude that the deletion of *Mtfp1* in hepatocytes confers direct protection to the liver against HFD-induced metabolic dysregulation by improving hepatocyte metabolism in a cell-autonomous manner.

***Mtfp1* deletion protects against hepatic cell death**

Given the previous implications of MTFP1 in cell death sensitivity reported in various cultured cell lines[17,19,28] and the association of MTFP1 and liver tumor progression in humans[29], we sought to directly test whether MTFP1 was involved in the regulation of cell survival in vivo. We measured the response to liver apoptosis by treating 3 month old mice for 24 hours with FAS antibodies, which specifically induces apoptotic liver damage via the activation of the FADD signaling pathway in a manner than is regulated by IMM integrity[30]. Macroscopically, the livers of WT mice treated with FAS showed hepatic damage characterized by the appearance of fibrotic and necrotic foci (Fig. 6A). FAS-induced liver damage resulted in a loss of liver mass (Fig. S6A), a dramatic increase of ALAT, ASAT and lactate dehydrogenase (LDH), a more general marker of tissue damage, by 35, 85 and 45-fold respectively in control livers (Fig. 6B, S6B). Hematoxylin and eosin (H&E) staining of control livers revealed tissue disruption, characterized by the presence of apoptotic bodies and hyper-eosinophilic cytoplasm, conferring large areas of architecture dysregulation (Fig. 6C), all of which features are consistent with apoptotic liver damage[15,23]. In contrast, H&E analyses of LMKO livers revealed far less FAS-induced damage (Fig. 6C) and plasma analyses revealed an 84% reduction of ALAT, an 86% reduction of ASAT, and a 97% reduction of LDH compared to FAS-injected control mice (Fig. 6B, Fig. S6B). Finally, TUNEL assays performed on histological liver sections demonstrated a profound reduction of cell death in FAS-treated LMKO mice compared to control mice (Fig. 6D). Taken together, these studies demonstrate that hepatocyte-specific *Mtfp1* depletion protects against apoptosis-induced liver damage in vivo.

To understand whether MTFP1 ablation protects hepatocytes from cell death in a cell-autonomous manner, we isolated primary hepatocytes from control and LMKO mice at 8-10 weeks of age and performed quantitative cell death assays ex vivo. To induce cell death, primary hepatocytes were treated with hydrogen peroxide (H_2O_2) [1mM] at 16 hours post plating and cell

bioRxiv preprint doi: https://doi.org/10.1101/2023.04.26.538374; this version posted April 28, 2023. The copyright holder for this preprint (which was not certified by peer review) is the author/funder, who has granted bioRxiv a license to display the preprint in perpetuity. It is made available under aCC-BY 4.0 International license.

death was by kinetically monitored by propidium iodide (PI) uptake using an automated live-cell imaging approach powered by supervised machine learning previously developed for cultured cell lines[31,32]. Consistent with our observations in vivo, *Mtfp1*$^{-/-}$ primary hepatocytes treated with H_2O_2 ex vivo showed a significant resistance against cell death (52% reduction at 4 hours) compared to control primary hepatocytes (Fig. 6E, F), arguing that MTFP1 ablation confers protection to autonomous hepatocyte death ex vivo. Programmed cell death in the liver, and more specifically in hepatocytes, can be tightly regulated through the opening of the mitochondrial permeability transition pore (mPTP)[32]. To test whether *Mtfp1* deletion impacted mPTP opening, we isolated hepatic mitochondria and simulated mPTP opening with calcium chloride overload (Fig. 6G). We observed a reduced sensitivity of mPTP opening in hepatic mitochondria isolated from LMKO mice compared to control littermates (Fig. 6G), which could be rescued by the pre-treatment with the mPTP inhibitor Cyclosporin A (CsA)[19]. Taken together, we conclude that *Mtfp1* deletion in hepatocytes confers protection against mPTP opening and cell death induction.

Discussion

Pre-clinical transgenic animal models have been instrumental in dissecting the underlying molecular remodeling of hepatocytes during the development of fatty liver disease and its sequelae. These studies have demonstrated the unassailable pathophysiological relevance of mitochondria, yet data from a large array knockout mice of mitochondrial genes have yielded a more complex picture: some hepatocyte-specific knockouts confer resistance to NAFLD/NASH while others inhibit normal liver function[33–37]. Pleotropic effects of the individual mitochondrial genes that were targeted in previous studies combined with the potential for metabolic cross-talk between tissues in vivo has made it challenging to pinpoint how modulating mitochondrial activity may be used to combat liver disease. Here, we discovered that Mitochondrial Fission Process 1 (MTFP1) plays an important role metabolic role in the liver of mice that is critical for NAFLD but not under basal conditions. MTFP1 was first identified as a metabolically-regulated inner mitochondrial membrane IMM) protein[16–18,33] initially implicated in mitochondrial fission and cell death resilience in a variety of cell lines[16–18,38]. In the liver, the discovery that MTFP1 protein expression is

bioRxiv preprint doi: https://doi.org/10.1101/2023.04.26.538374; this version posted April 28, 2023. The copyright holder for this preprint (which was not certified by peer review) is the author/funder, who has granted bioRxiv a license to display the preprint in perpetuity. It is made available under aCC-BY 4.0 International license.

predictive of hepatocellular carcinoma survival and recurrence risk in humans[15], prompted us to directly investigate its role in the liver.

Here, we created Liver-specific *Mtfp1* knockout (LMKO) mice (Fig. 1A-E, S1A,B) by expressing a hepatocyte-specific Cre-recombinase[39] in a conditional mouse model of *Mtfp1*[15]. We discovered that LMKO mice are healthy and virtually indistinguishable from littermate control mice, showing no defects in liver function and no indication of liver damage nor inflammatory responses and liver RNAseq analyses only showed 0.1% of genes were dysregulated, none of which were involved in pathogenic hepatic remodeling (Fig. 1, S1). While the livers of LMKO mice appeared unchanged, characterization of hepatic mitochondria revealed two major functional improvements: increased respiratory capacity and resistance to permeability transition pore opening. High resolution fluor-respirometry measurements of MTFP1-deficient liver mitochondria showed increased ADP-stimulated (state 3) oxygen consumption rates under all substrates we tested, which was associated a commensurate increase in the specific activities of complex IV and complex V (Fig. 2B-F). Quantitative label-free proteomic studies revealed a ratio-metric increase in the levels of Complex V subunits, which paralleled the increased levels of assembled Complex V detected by BN-PAGE, pointing to an increased assembly and/or maintenance of the ATP synthase complex (Fig. 2G-I). Enhanced respiration was not associated with proton leak (Fig. 2B,C) nor cristae alterations (Fig. S2D) that we reported in MTFP1-deficient hearts[34], leaving us wondering: how does MTFP1 ablation enhance OXPHOS activity and mitochondrial coupling and do so specifically in the liver?

The spare respiratory capacity of hepatocytes has been reported to supersede that of cardiomyocytes, indicating that under basal conditions cardiomyocyte mitochondria are working far closer to their maximal capacity[40]. In contrast, morphometric studies of cardiac mitochondria from rodents reveal cristae densities that approach the physical and functional limits exemplified by tuna[41] and hummingbird hearts[42], consistent with the notion that there may be little additional IMM real estate upon which to build additional OXPHOS complexes in the heart[43]. In the liver, mitochondria have a comparatively reduced IMM density, OXPHOS protein content[44], and IMM protein half-lives[45] and would therefore be capable of increasing OXPHOS complex assembly to enhance mitochondrial coupling and respiration. In rodents, systemic thyroid hormone injections

bioRxiv preprint doi: https://doi.org/10.1101/2023.04.26.538374; this version posted April 28, 2023. The copyright holder for this preprint (which was not certified by peer review) is the author/funder, who has granted bioRxiv a license to display the preprint in perpetuity. It is made available under aCC-BY 4.0 International license.

can increase hepatocyte cristae density to increase the content and activity of the respiratory chain[46,47]. On the other hand, genetic models of obesity manifest the oppositive effect, with altered cristae organization in swollen mitochondria and reduced levels of cytochrome *c* oxidase[48], which we also confirmed by proteomic studies of HFD-fed control mice (Fig. S4A, B). Yet to the best of our knowledge, LMKO mice represent the first genetic mouse model that elevates respiration by increasing the activity of Complex IV and V rather than by boosting total mitochondrial mass or by promoting uncoupling.

MTFP1 ablation in the liver enhances state 3 respiration regardless of the substrate source (Fig. 2B) yet this increase is most profound when the palmitoyl-carnitine is supplied in excess, as evidenced by the increased respiratory control ration (RCR) in the presence of fatty acids but not carbohydrate-derived substrates (Fig. 2B), revealing that MTFP1-deficient liver mitochondria are capable of coupling voracious beta enhanced OXPHOS activity. A clear prediction of increased beta oxidation capacity of hepatocyte mitochondria is an enhanced propensity to metabolize excess lipids and therefore a resistance against diet-induced hepatic steatosis in vivo[1]. Indeed, when we challenged LMKO mice with a long-term a high fat diet (HFD), they showed remarkable resistance to fatty liver disease and metabolic dysregulation despite equal levels of food consumption and in-cage activity. Metabolic protection appears to be restricted to the liver, as LMKO mice were not protected against the increased extra-hepatic adiposity, dysregulated systemic glucose metabolism, and aberrant glucose-stimulated insulin secretion by the pancreas that caused by HFD feeding. Mimicking diet-induced steatosis in the tissue culture dish with primary hepatocytes isolated from NCD-fed mice, we could show that excessive lipid droplet accumulation was blunted in *Mtfp1*$^{-/-}$ primary hepatocytes ex vivo that is consistent with enhanced mitochondrial coupling in these cells (Fig. 5H).

The discovery that MTFP1 ablation in the liver is benign and even beneficial under stress conditions is in stark contrast to our recent report that *Mtfp1* deletion in cardiomyocytes causes heart failure[43]. However, defects in inner membrane integrity observed in *Mtfp1*$^{-/-}$ cardiac mitochondria were not observed in *Mtfp1*$^{-/-}$ liver mitochondria: membrane potential was maintained (Fig. 2C) and mPTP was increased rather than decreased (Fig. 6G). Moreover, the livers of LMKO mice show increased mitochondrial respiratory capacity (Fig. 2B) and no signs of cell death or

bioRxiv preprint doi: https://doi.org/10.1101/2023.04.26.538374; this version posted April 28, 2023. The copyright holder for this preprint (which was not certified by peer review) is the author/funder, who has granted bioRxiv a license to display the preprint in perpetuity. It is made available under aCC-BY 4.0 International license.

inflammation (Fig. 4I, S3A), while MTFP1 deficiency in the heart triggered cardiomyocyte death, fibrotic remodeling, and heart failure[15]. At first, we found these physiological discrepancies perplexing, since the heart and liver are both rely heavily on mitochondria yet further exploration of the literature provided conspicuous examples demonstrating that these two organs can in fact respond differently to mitochondrial dysfunction. For example, ablation of Complex I activity in the cardiomyocytes can cause a fatal hypertrophic cardiomyopathy in mice[49] while its ablation in hepatocytes does not impact liver structure and function[37]. Similarly, interfering with the activity of the mitochondrial fusion proteins OPA1[50,51] or Mitofusins[52] specifically in cardiomyocytes yields disastrous outcomes for cardiac function, yet in doing so in the liver is either benign[33,34] or even advantageous against NASH[35]. Similarly, cardiac deletion of the adenine nucleotide transporter elicits cardiac hypertrophy but in the liver, its genetic or biochemical inhibition in the liver can be beneficial, protecting against hepatic steatosis and metabolic dysregulation[36,53]. In mice, system-wide disruption of mitochondrial genes such as *Chchd10*[54,55], *Dnm1l*[56], *Wars2*[57], and *Cox1*[58] can trigger multi-organ dysfunction in which the liver, but not the heart, is spared, further illustrating that the liver may respond differently (or not at all) to genetic insults otherwise catastrophic to other tissues.

But why does the ablation of MTFP1 impact liver mitochondria so differently? It is likely that divergent cell type-specific effects reflect the different metabolic, structural, and functional characteristics of mitochondria they harbor. Indeed, compelling differences between the heart and liver have been documented at the level of mitochondrial network morphology, IMM and cristae organization[59], mitochondrial proteome composition and protein half-lives[45], OXPHOS complex organization and assembly[60], substrate utilization and enzymatic activities of the respiratory chain[60,61], and even the molecular regulation of the mPTP[61–65]. Consistent with these observations, we found little overlap between the differentially expressed mitochondrial genes and proteins of knockout hearts and livers: no genes besides *Mtfp1* were commonly dysregulated between both knockout tissues while only 13% (35 out of 264 proteins) shared common differential expression patterns (Fig. S7). MTFP1 interactomes were also remarkably dissimilar, with only 7 out of 113 interacting partners of liver MTFP1 found to overlap with the cardiac MTFP1 interactome. MTFP1 is devoid of conserved motifs or catalytic domains and forms a complex of approximately 150kDa,

bioRxiv preprint doi: https://doi.org/10.1101/2023.04.26.538374; this version posted April 28, 2023. The copyright holder for this preprint (which was not certified by peer review) is the author/funder, who has granted bioRxiv a license to display the preprint in perpetuity. It is made available under aCC-BY 4.0 International license.

which is significantly smaller than the fully assembled mito-ribosome and ATP synthase complexes with whose subunits it interacts and thus we posit that the impacts on mitochondrial function that result from the ablation MTFP1 may reflect its role as a protein scaffold in the IMM. Indeed, MTFP1 co-migrates with both adenine nucleotide translocase (ANT1) and Cyclophilin D (encoded by *Ppif*), both of which have been previously physically and functionally connected to mitochondrial ATP synthesis[62–66] and the mPTP. Our data also support a role for MTFP1 as a regulator of mPTP activity in the liver, as inactivation of hepatocytes slows mPTP opening response in liver mitochondria and protects against liver cell death in primary hepatocytes and in mice (Fig. 6). This pro-survival role of MTFP1 in the liver appears to be independent from the metabolic protection its deletion confers against HFD-induced hepatic steatosis, since HFD-feeding does not cause cell death (Fig. 4I).

The metabolic protection conferred to MTFP1-deficient livers that are already hyper-proficient in mitochondrial respiration and fatty acid oxidation is best appreciated under chronic HFD feeding. Intriguingly, recombinant inbred mouse models that are susceptible to NAFLD/NASH show a downregulation of *Mtfp1* expression in the liver while those that are resistant do not[67]. While diet-induced hepatic steatosis predisposes humans to NASH and cirrhosis, HFD-feeding alone does trigger NASH in laboratory mice so we have not yet learned whether LMKO mice are protected from the downstream sequelae of hepatic steatosis. Nevertheless, LMKO mice have availed themselves to be a unique tool to understand how enhancing mitochondrial respiration can combat metabolic liver disease and will undoubtedly prove useful for the in vivo exploration and development of therapeutic targets for other inherited and acquired liver diseases.

Materials and Methods

Animals

Animals were handled according to the European legislation for animal welfare (Directive 2010/63/EU). All animal experiments were performed according to French legislation in compliance with the European Communities Council Directives (2010/63/UE, French Law 2013-118, February 6, 2013) and those of Institut Pasteur Animal Care Committees (CETEA is Comité

bioRxiv preprint doi: https://doi.org/10.1101/2023.04.26.538374; this version posted April 28, 2023. The copyright holder for this preprint (which was not certified by peer review) is the author/funder, who has granted bioRxiv a license to display the preprint in perpetuity. It is made available under aCC-BY 4.0 International license.

d'Ethique en Expérimentation Animale 89). The specific approved protocol number is #20687-2019051617105572. Mice were housed within a specific pathogen free facility and maintained under standard housing conditions of a 14-10h light-dark cycle, 50-70% humidity, 19-21°C with free access to food and water in cages enriched with bedding material and gnawing sticks. Alb-Cre recombinase[39] and mitoYFP[68] mouse lines are commercially available (MGI: 2176946 and 5292496). The *Mtfp1* conditional mouse model[68] was generated by PolyGene on a C57Bl/6N genetic background using two LoxP sites and an FRT-flanked neomycin cassette. The first LoxP site and neomycin resistance cassette is located in intron 1 and the second LoxP site is inserted in intron 3. The FRT-flanked neomycin cassettes were removed *in vivo* by Flp-recombination by crossing to Flp-deleter breeding step. Hepatocyte specific FLAG-MTFP1 Knock-In (KI) mice (*Alb-Cre*$^{tg/+}$*Mtfp1*$^{+/+}$*, CAG*$^{tg+/}$*)* were generated by crossing an inducible mouse model for mCherry-P2A-FLAG-MTFP1[69] generated by PolyGene AG (Switzerland) on a C57Bl6/N background expression under the CAG promoter with mice expressing the Cre recombinase under the control of the hepatocyte-specific albumin Cre promoter. Liver specific *Mtfp1* knockout mice (LMKO) were generated by mating AlbCre+ mice with *Mtfp1*$^{LoxP/LoxP}$ mice, this led to the deletion of flanked region containing exons 2 and 3 (925 bp in total), resulting in the loss of the majority of the coding region of *Mtfp1* and a loss of *Mtfp1* expression. For fluoresce microscopy analysis of primary hepatocytes the triple transgenic line AlbCre+; mitoYFP+; *Mtfp1*$^{LoxP/LoxP}$ was generated.

Mice were fed a normal chow diet (NCD, Teklad global protein diet; 20% protein, 75% carbohydrate, 5% fat) or high fat diet (HFD) containing 22 kJ% carbohydrates 24 kJ% protein and 54 kJ% fat (Ssniff® EF acc. E15742-347) for 16 weeks starting from the age of 8 weeks. During the treatment mice were monitored weekly for the body weight and every other week for the glycaemia, which was measured using a glucometer (Accu-Chek Performa, Roche, 1486023). To induce hepatic cell death, Fas antigen, CD95 (BD BioSciences, 554254) was intra-peritoneal injected in 18-hour fasted mice at the concentration of 225µg/kg (BW). Mice were sacrificed 24 hours post injection.

Mouse genotype was determined at weaning. For the genotyping, genomic DNA was isolated from mouse tail snip using lysis buffer Tris-HCl (EuroMedex, 26-128-3094-B) pH8.5 100mM; Ethylenediaminetetraacetic acid (EDTA, 5mM; EuroMedex, EU0084-B); Sodium Dodecyl Sulfate

bioRxiv preprint doi: https://doi.org/10.1101/2023.04.26.538374; this version posted April 28, 2023. The copyright holder for this preprint (which was not certified by peer review) is the author/funder, who has granted bioRxiv a license to display the preprint in perpetuity. It is made available under aCC-BY 4.0 International license.

(SDS, 0.2%; EuroMedex, 1833); Sodium Chloride (NaCl, 200mM; EuroMedex, 1112-A); Proteinase K 400µg/ml (Sigma-Aldrich, 03115879001); samples were incubated at 56°C until digested and then centrifuged for 3 min at 16000g. Supernatants were transferred to fresh tubes, and DNA was precipitated first with 1000 µl of isopropanol, centrifuged at 16000g for 10 minutes at 4°C, pellet were washed with 500 µl of 70% ethanol, centrifuged at 16000g for 10 minutes at 4°C, and DNA was resuspended in H_2O. PCR was performed using the 5x Hot FIREpol (SOLIS BIODYNE, 755015) at 94°C for 3 minutes, (94°C for 15 seconds, 55°C 30 seconds, 72°C for 1 minute) for 35 cycles, 72°C for 7 minutes and 4°C. Primers used for genotyping are listed in Supplemental Dataset 4.

Metabolic studies

Food and water intake, respiratory exchange ratio (RER), and physical activity were tested for 5 days using the PhenoMaster system (TSE Systems, Bad Homburg, Germany), which allowed continuous undisturbed and controlled recording. during day and night periods. 5 days before the recording, the animals were placed in the room and in cages similar to the PhenoMaster cages, for acclimatization. The following parameters were recorded every 3 minutes and averaged hourly or for the light and dark phase as indicated: food consumption (g), water consumption (ml), distance covered (cm), and RER (ratio between the amount of carbon dioxide (CO_2) produced in metabolism and oxygen (O_2) used). RER has a range from 0.7 to 1.0 according to the fuel source, when close to 0.7 means that fats are the predominant source, closest to 1.0, carbohydrates are predominantly consumed.

For Pyruvate Tolerance Test (IP-PTT): 18-hour fasted mice were administered intra-peritoneal injections of sterile pyruvate (Sigma-Aldrich, P2256) at 1 g/kg (BW). Glucose and Insulin Tests for Glucose Tolerance Test (IP-GTT): 18-hour fasted mice were administered intra-peritoneal injections of sterile glucose (EuroMedex, UG3050) at 2 g/kg. For Insulin Tolerance Test (IP-ITT): 6-hour fasted mice were administered intra-peritoneal injections of Insulin aspart (NovoRapid) at 1 g/kg (BW). For all the tests, blood glucose levels were measured before injection and 15, 30, and 60 post-injection using a glucometer (Accu-Chek Performa, Roche). For glucose-stimulated insulin production, mice were fasted for 18 hours and were administered intra-peritoneal injections of

bioRxiv preprint doi: https://doi.org/10.1101/2023.04.26.538374; this version posted April 28, 2023. The copyright holder for this preprint (which was not certified by peer review) is the author/funder, who has granted bioRxiv a license to display the preprint in perpetuity. It is made available under aCC-BY 4.0 International license.

sterile glucose (EuroMedex, UG3050) at 2 g/kg. Insulin levels were analyzed by ELISA (Crystal Chem, 90082).

Whole blood was collected from the submandibular vein of awake mice in tubes containing heparin (Sigma-Aldrich, H4784) at the concentration of 50U/ml and centrifuged at 3000g for 10 minutes at 4°C to isolate plasma. Plasma analyses of transaminases (ASAT and ALAT), LDH, cholesterol and triglycerides (TG) were performed by the 'Microdosages biochimiques' at the 'Institut de Physiologie et Pathologie, Claude Bernard' core facility (Paris).

Analysis of body composition

Fat and lean mass were determined in awake Control and LMKO mice by nuclear magnetic resonance (NMR) using the Contactless Check Weighing (CCW) by MiniSpec MQ (Bruker MiniSpec Plus) with a 0.15-T magnetic field and a 6.2-MHz frequency pulse. This device measures the mass of fat, lean tissue, and fluid based on prior calibration. Mice were placed in an acrylic cylinder (48-mm diameter) and was loosely restrained within the cylinder by pushing a plunger. The cylinder was then positioned inside the bore of the magnet maintained at constant temperature of 37°C. The measurements were recorded as % of fat, lean, and fluids.

Tissue analyses

Histological and morphometric analysis: liver and white adipose tissue were fixed with phosphate-buffered 10% formalin (Sigma-Aldrich, F5554) for 20 hours then washed in 70% ethanol, then embedded in paraffin, sectioned by microtome (4 um) and stained with hematoxylin & eosin. Cell death was assessed using the TUNEL assay kit – HRP – DAB (AbCam, ab206386). All slides were scanned using the Slide scanner Axio Scan.Z1 (ZEISS). Representative pictures were obtained using the CZI software (Zen 2.3 lite; ZEISS).

Triglyceride assay: snap frozen liver tissue was used to assess hepatic triglyceride content by fluorometric assay (AbCam, ab178780).

Isolation of mitochondria

Livers were gently homogenized on ice in Mitochondria Isolation Buffer (MIB: Sucrose 275mM (EuroMedex, 200-301-b); ethylene glycol tetra acetic acid (EGTA-KOH pH7 1mM; EuroMedex,

bioRxiv preprint doi: https://doi.org/10.1101/2023.04.26.538374; this version posted April 28, 2023. The copyright holder for this preprint (which was not certified by peer review) is the author/funder, who has granted bioRxiv a license to display the preprint in perpetuity. It is made available under aCC-BY 4.0 International license.

E4378) Tris pH 7.4 20mM; Bovine Serum Albumin (free fatty acid BSA, 0.25 mg/ml; Sigma-Aldrich, A6003) and protease inhibitors (Roche). Differential centrifugation at 1000g for 10 minutes at 4°C yielded supernatant that was subsequently centrifuged at 3000g for 15 minutes at 4°C. The resulting crude mitochondrial pellet fraction was resuspended in MIB and protein concentration was quantified with Bradford assay (Sigma-Aldrich, B6916) using a spectrophotometer (Infinite 200 Pro, Tecan). Isolated mitochondria were used for Blue-Native Polyacrylamide Gel Electrophoresis (BN-PAGE), SDS-PAGE or for High-Resolution Respirometry (HRR) assays.

High Resolution Respirometry

Mitochondrial oxygen consumption was measured with an Oxygraph-2k (Oroboros Instruments, Innsbruck, AT). 50 to 500 µg of mitochondria were diluted in 2.1 ml of mitochondrial respiration buffer (Magnesium Chloride ($MgCl_2$, 3mM; Sigma-Aldrich, M3634); Lactobionic Acid 60mM (Sigma-Aldrich, 153516); Taurine 20mM (Sigma-Aldrich, T0625); Potassium phosphate monobasic (KH_2PO_4, 10mM; EuroMedex, 2018); 4-(2-Hydroxyethyl)piperazine-1-ethanesulfonic acid, N-(2-Hydroxyethyl)piperazine-N′-(2-ethanesulfonic acid) (HEPES-KOH pH 7.4 20 mM; EuroMedex, 10-110); Sucrose 110mM; EGTA-KOH pH7 0.5mM and free fatty acid BSA 1g/l). To ensure mitochondrial quality and integrity, cytochrome *c* (CytC, 2µM;Sigma-Aldrich, C7752) was used. The oxygen consumption (JO_2) rate was measured using either Pyruvate 10mM, Glutamate 5mM (Sigma-Aldrich, G1626) and Malate 5mM (Sigma-Aldrich, M1000), or Palmitoyl-Carnitine (PC, 25uM; Sigma-Aldrich, P1645). To specifically assess Complex II activity, Rotenone 0.5 µM (Sigma-Aldrich, R8875) and Succinate 10mM (Sigma-Aldrich, S2378) were used as substrates. Oxygen consumption was assessed in the phosphorylating state with Adenosine 5′-diphosphate monopotassium salt dihydrate (ADP, 0.2 mM; Sigma-Aldrich, A5285) or non-phosphorylating state by adding oligomycin (OLGM, 5 µM, Sigma-Aldrich, O4876).

The cytochrome *c* oxidase (COX) activity was measured in the presence of Ascorbate-Na (2mM; Sigma-Aldrich, A4034; pH6 with Ascorbic acid (Sigma-Aldrich, A7506)) and N,N,N′,N′-Tetramethyl-p-phenylenediamine dihydrochloride (TMPD, 0.5mM; Sigma-Aldrich, 87890), with prior inhibition with Antimycin A (AMA, 2,5µM; Sigma-Aldrich, A8674), finally KCN (2mM, Sigma-Aldrich, 60178) was injected to evaluate the effective complex IV-dependent respiration.

bioRxiv preprint doi: https://doi.org/10.1101/2023.04.26.538374; this version posted April 28, 2023. The copyright holder for this preprint (which was not certified by peer review) is the author/funder, who has granted bioRxiv a license to display the preprint in perpetuity. It is made available under aCC-BY 4.0 International license.

The ATPase activity was assessed by colorimetric assay. Mitoplasts were incubated for 15 minutes in the following buffer: triethanolamine 75mM (Sigma-Aldrich, T58300), $MgCl_2$ 2mM pH8.9 followed by the addition of ATP 5mM (Sigma-Aldrich, A6419) or ATP 5mM and Oligomycin 5µM (to determine the oligomycin-insensitive ATPase activity) or ADP 5mM (used as negative control).

Mitochondrial swelling assay

Mitochondrial permeability transition pore opening was monitored by calcium-induced mitochondrial swelling and change of light scattering (absorbance 540 nm). Freshly isolated hepatic mitochondria from control and LMKO mice aged 8-10 week were resuspended in Ca^{2+} uptake buffer (120mM KCl, 5mM MOPS, 5mM KH_2PO_4, 10mM Glutamate, 5mM Malate, pH 7.4 in presence of cOmplete™ EDTA-free Protease Inhibitor Cocktail (Sigma 4693132001) at a concentration of 500 µg/mL and stimulated by the addition of a single pulse of 125µM $CaCl_2$. The absorbance at 540 nm was measured at intervals of 30 seconds for 20 minutes at 37°C using the microplate reader (Tecan). Cyclosporin A (1µM) was used to inhibit the mPTP opening.

BN-PAGE of liver mitochondria

1D BN-PAGE was performed as described previously[69] with some modifications. Briefly, liver mitochondria (100 µg, mitochondrial protein concentration was determined with DC Protein Assay BIO-RAD) were isolated from control and LMKO mice and incubated with digitonin extraction buffer (HEPES (30mM), potassium Acetate (150 mM), Glycerol (12%), 6-Aminocaproic acid (2mM), EDTA (2mM), high purity digitonin (4.5g/g), pH=7.2). Mitochondria were vortexed 1 hour at 4ºC to solubilize membranes and after centrifugated at 21,000 g for 30 minutes. Supernatants were transferred to a new tube and mixed with loading dye (0.0124% (w/v), Coomassie brilliant blue G-250 (InVitroGen, BN2004)). Digitonin solubilized mitochondria were loaded 3-12% Bis-Tris Invitrogen™ Novex™ NativePAGE™ 3-12% acrylamide gel (1mm) (Invitrogen, BN2011BX10) using the anode running buffer (Invitrogen, BN2001) and Cathode Buffer Additive (0.5%) added to the anode buffer (Invitrogen, BN2002). Samples were migrated at 80V 20mA for 45 minutes and at 150V 20 mA for 13 hours. Gel was incubated in Transfer buffer (Tris (0.304% w/v), Glycine (1.44% w/v)) plus SDS (0.2% v/v) and β-mercaptoetanol (0.2% v/v)) for 30 minutes at room temperature

bioRxiv preprint doi: https://doi.org/10.1101/2023.04.26.538374; this version posted April 28, 2023. The copyright holder for this preprint (which was not certified by peer review) is the author/funder, who has granted bioRxiv a license to display the preprint in perpetuity. It is made available under aCC-BY 4.0 International license.

(RT) to denature proteins. After the incubation, gels were transferred on polyvinylidene difluoride (PVDF) in transfer buffer (Tris (0.304% w/v), Glycine (1.44% w/v), Ethanol (10%v/v)) at 400mA 20V for 3 hours and 30 minutes. After transfer, membranes were washed with methanol to remove Coomassie blue staining. For immunodetection, membranes were blocked with 5% milk in Tween-Tris-buffered saline (TTBS) for 1 hour at RT and incubated overnight with the specific primary antibody diluted in blocking solution. The membrane was washed three times in TTBS and incubated for 2 hours at RT with the appropriate secondary antibody conjugated with horseradish peroxidase (HRP). Finally, membranes were incubated in Tris-HCL (0.1 M pH 8.5) plus Luminol and p-Coumaric acid for 3 minutes and luminescence was detected using a ChemiDoc TM XRS+Imaging System. Band intensity was determined with Image Lab Software

For 2D BN-PAGE, first dimension native gels were incubated in MOPS1x SDS Running Buffer (Fished Scientific) supplemented with β-mercaptoetanol (0.2% v/v) for 30 minutes at RT and then run in a denaturing second dimension electrophoresis (2D-SDS PAGE). The gels were run in MOPs buffer and then transferred to a nitrocellulose membrane. Immunodetection was performed as previously described. Primary antibodies used for immunoblotting of BN-PAGE are listed in Supplemental Dataset 4.

Protein extraction, immunoblotting and immunoprecipitation

To prepare total cell lysates for immunoblot analysis, cells were washed twice with cold Dulbecco's Phosphate-Buffered Saline (PBS; GIBCO, 14190169), scraped from the dishes and collected in tubes, then centrifuged at 16000g for 10 minutes at 4°C. For liver samples, tissue was pulverized or isolated mitochondria were spun at 3000g for 10 minutes at 4°C. Cell or mitochondria pellet or tissue powder were resuspended in RIPA buffer (Tris pH 7.4 50mM; NaCl 150 mM; Triton X-100 (EuroMedex, 2000C) 1%; Sodium Deoxycholate 0.05% (Sigma-Aldrich, D6750); SDS 0.10%; EDTA 1 mM; protease inhibitors and PhosphoStop Inhibitors (Roche), homogenized with a pestle (Eppendorf, 033522) and incubated at 4°C for 30 minutes on a rotating wheel, then spun at 16000g for 10 minutes. Protein concentration was determined with Bradford assay using a plate reader (TECAN). Protein extracts were prepared in Laemmli Buffer (Bio-Rad, 1610747) with 2-

bioRxiv preprint doi: https://doi.org/10.1101/2023.04.26.538374; this version posted April 28, 2023. The copyright holder for this preprint (which was not certified by peer review) is the author/funder, who has granted bioRxiv a license to display the preprint in perpetuity. It is made available under aCC-BY 4.0 International license.

Mercaptoethanol 355mM (Sigma-Aldrich, M3148) and boiled at 95°C for 5 minutes, then resolved by SDS-PAGE (Mini Protean chamber and TGX gels, Bio-Rad) and transferred onto nitrocellulose membrane (Trans-blot Turbo Transfer system and kit, Bio-Rad) followed by blocking with 3% milk for 30 minutes. Membranes were then incubated with the primary antibodies (listed in Table 2) and HRP-linked secondary antibodies (anti-mouse or anti-rabbit IgG; Thermo Fisher Scientific, 10368172 and 11034). Clarity Western ECL (Bio-Rad) was used for the detection with ChemiDoc (Bio-Rad). Densitometric analysis of immunoblots was performed using Image Lab software (Bio-Rad). The signal of the quantified bands was normalized to loading controls or Stain-free TGX staining as indicated[70] and presented as fold difference over control treatment or control genotype as the invariant control.

Proteomics

Liver extract proteins were extracted and denatured in RIPA buffer. Samples were sonicated using a Vibracell 75186 and a miniprobe 2 mm (Amp 80% // Pulse 10 off 0.8, 3 cycles) and further centrifuged. Protein assay was performed on supernatant (Pierce 660 nm, according to manufacturer instructions) and 100 µg of each extract was delipidated and cleaned using a Chloroform / Methanol / Water precipitation method. Briefly, 4 volume of ice-cold methanol were added to the sample and vortex, 2 volume of ice-cold chloroform were added and vortex and 3 volume of ice-cold water was added and vortex. Samples were centrifuged 5 min at 5000 g. The upper layer was removed and proteins at the interface were kept. Tubes were filled with ice-cold methanol and centrifuged at max speed for 5 min. Resulting protein pellet was air-dried and then dissolved in 130 µl of 100mM NaOH before adding 170 µl of Tris 50 mM pH 8.0, tris (2-carboxyethyl)phosphine (TCEP) 5 mM and chloroacetamide (CAA) 20 mM. The mixture was heated 5 min at 95 °C and then cooled on ice. Endoprotease LysC (1µg) was use for an 8h digestion step at (37° C) followed with a trypsin digestion (1 µg) at 37°C for 4 h. Digestion was stopped adding 0.1% final of trifluoroacetic acid (TFA). Resulting peptides were desalted using a C18 stage tips strategy (Elution at 80% Acetonitrile (ACN) on Empore C18 discs stacked in a P200 tips) and 30 µg of peptides were further fractionated in 4 fractions using poly(styrenedivinylbenzene) reverse phase sulfonate (SDB-RPS) stage-tips method as previously

bioRxiv preprint doi: https://doi.org/10.1101/2023.04.26.538374; this version posted April 28, 2023. The copyright holder for this preprint (which was not certified by peer review) is the author/funder, who has granted bioRxiv a license to display the preprint in perpetuity. It is made available under aCC-BY 4.0 International license.

described[71,72]. Four serial elutions were applied as following: elution 1 (80 mM Ammonium formate (AmF), 20% (v/v) ACN, 0.5% (v/v) formic acid (FA)), elution 2 (110 mM AmF, 35% (v/v) ACN, 0.5% (v/v) FA), elution 3 (150 mM AmmF, 50% (v/v) ACN, 0.5% (v/v) FA) and elution 4 (80% (v/v) ACN, 5 % (v/v) ammonium hydroxide). All fractions were dried and resuspended in 0.1% FA before injection.

NanoLC-MS/MS

LC-MS/MS analysis of digested peptides was performed on an Orbitrap Q Exactive Plus mass spectrometer (Thermo Fisher Scientific, Bremen) coupled to an EASY-nLC 1200 (Thermo Fisher Scientific). A home-made column was used for peptide separation (C_{18} 50 cm capillary column picotip silica emitter tip (75 µm diameter filled with 1.9 µm Reprosil-Pur Basic C_{18}-HD resin, (Dr. Maisch GmbH, Ammerbuch-Entringen, Germany)). It was equilibrated and peptide were loaded in solvent A (0.1 % FA) at 900 bars. Peptides were separated at 250 $nl.min^{-1}$. Peptides were eluted using a gradient of solvent B (ACN, 0.1 % FA) from 3% to 7% in 8 min, 7% to 23% in 95 min, 23% to 45% in 45 min (total length of the chromatographic run was 170 min including high ACN level step and column regeneration). Mass spectra were acquired in data-dependent acquisition mode with the XCalibur 2.2 software (Thermo Fisher Scientific, Bremen) with automatic switching between MS and MS/MS scans using a top 12 method. MS spectra were acquired at a resolution of 35000 (at *m/z* 400) with a target value of 3×10^6 ions. The scan range was limited from 300 to 1700 *m/z*. Peptide fragmentation was performed using higher-energy collision dissociation (HCD) with the energy set at 27 NCE. Intensity threshold for ions selection was set at 1×10^6 ions with charge exclusion of z = 1 and z > 7. The MS/MS spectra were acquired at a resolution of 17500 (at *m/z* 400). Isolation window was set at 1.6 Th. Dynamic exclusion was employed within 45 s.

Data Processing

Data were searched using MaxQuant (version 1.5.3.8) using the Andromeda search engine[73] against a reference proteome of Mus musculus (53449 entries, downloaded from Uniprot the 24th of July 2018). The following search parameters were applied: carbamidomethylation of cysteines was set as a fixed modification, oxidation of methionine and protein N-terminal acetylation were set as variable modifications. The mass tolerances in MS and MS/MS were set to 5 ppm and 20 ppm respectively. Maximum peptide charge was set to 7 and 5 amino acids were required as minimum

bioRxiv preprint doi: https://doi.org/10.1101/2023.04.26.538374; this version posted April 28, 2023. The copyright holder for this preprint (which was not certified by peer review) is the author/funder, who has granted bioRxiv a license to display the preprint in perpetuity. It is made available under aCC-BY 4.0 International license.

peptide length. A false discovery rate of 1% was set up for both protein and peptide levels. All 4 fractions per sample were gathered and the iBAQ intensity was used to estimate the protein abundance within a sample[74].

The label-free quantitative (LFQ) proteomics data was annotated in Perseus v.1.6.14.0[75] with Mouse MitoCarta 3.0[77] for individual OXPHOS complexes, mitoribosome and whole mitochondria using uniprot IDs. The Relative Complex Abundance (RCA) of the OXPHOS and mitoribosome were plotted with an in-house R script (R v.4.0.3, R studio v.1.3.1093) correcting for differential mitochondrial content using the ratio mean of LFQ values of mitochondria "+" annotations from MitoCarta 3.0. The mean of normalized values and standard deviation were calculated for each subunit of each complex comparing the LMKO and control mouse values from quantitative proteomics data along with the 95% confidence interval based on the t-statistic for each complex. A paired t-test calculated the significance between the LMKO and control mouse values for each complex. P-value *** = $p \leq 0.001$, ns= non-significant.

Mass spectrometry data have been deposited at the ProteomeXchange Consortium (http://www.proteomexchange.org) via the PRIDE partner repository[76,77] with the dataset identifier PXD041197.

Co-Immunoprecipitation assay

500 µg of cardiac liver mitochondria were freshly isolated from heart tissue of cardiomyocyte specific Flag-MTFP1 Knock-In (KI) mice (*Alb-Cre$^{tg/+}$Mtfp1$^{+/+}$, CAG$^{tg+/}$)* and Control mice (*Albe-Cre$^{+/+}$Mtfp1$^{+/+}$, CAG$^{tg/+}$)* as described above. Mitochondria were lysed in IP buffer (20 mM HEPES-KOH pH 7.5, 150 mM NaCl, 0.25% Triton X-100, protease inhibitor cocktail) on ice for 20 min and then centrifugated at 10000 g, 4°C for 15 min. Supernatant obtained by centrifugation was then incubated with 20 µL of anti-FLAG magnetic beads (Sigma M8823) for 2 hours at 4°C. The immunocomplexes were then washed with IP buffer without Triton X-100 and eluted with Laemmli Sample Buffer 2x at 95°C for 5 min. Protein were stacked in a 15 % SDS-PAGE gel with a 10 min long migration at 80 V. Proteins were fixed in gel and migration was visualized using the Instant Blue stain (Expedeon). Bands were excised for digestion. Gel bands were washed twice in Ammonium bicarbonate (AmBi) 50 mM, once with AmBi 50 mM / ACN 50 % and once with 100%

bioRxiv preprint doi: https://doi.org/10.1101/2023.04.26.538374; this version posted April 28, 2023. The copyright holder for this preprint (which was not certified by peer review) is the author/funder, who has granted bioRxiv a license to display the preprint in perpetuity. It is made available under aCC-BY 4.0 International license.

ANC. Gel band were incubated for 30 min at 56°C in 5 mM dithiothreitol (DTT) solution for reduction. Gel bands were washed in AmBi 50 mM and then in 100% ACN. Alkylation was performed at room temp in the dark by incubation of the gel bands in Iodocateamide 55 mM solution. Gel bands were washed twice in AmBi 50mM and in 100% ACN. 600 ng of trypsin were added for 8h digestion at 37°C. Peptides were extracted by collecting 3 washes of the gel bands using AmBi 50 mM / 50 % ACN and 5 % FA. Peptides clean up and desalting was done using Stage tips (2 disc Empore C18 discs stacked in a P200 tip).

LC-MS/SM analysis of digested peptides was performed on an Orbitrap Q Exactive HF mass spectrometer (Thermo Fisher Scientific, Bremen) coupled to an EASY-nLC 1200 (Thermo Fisher Scientific). A home-made column was used for peptide separation (C_{18} 30 cm capillary column picotip silica emitter tip (75 µm diameter filled with 1.9 µm Reprosil-Pur Basic C_{18}-HD resin, (Dr. Maisch GmbH, Ammerbuch-Entringen, Germany)). It was equilibrated and peptide were loaded in solvent A (0.1 % FA) at 900 bars. Peptides were separated at 250 $nl.min^{-1}$. Peptides were eluted using a gradient of solvent B (ACN, 0.1 % FA) from 3% to 26% in 105 min, 26% to 48% in 20 min (total length of the chromatographic run was 145 min including high ACN level step and column regeneration). Mass spectra were acquired in data-dependent acquisition mode with the XCalibur 2.2 software (Thermo Fisher Scientific, Bremen) with automatic switching between MS and MS/MS scans using a top 12 method. MS spectra were acquired at a resolution of 60000 (at *m/z* 400) with a target value of 3×10^6 ions. The scan range was limited from 400 to 1700 *m/z*. Peptide fragmentation was performed using HCD with the energy set at 26 NCE. Intensity threshold for ions selection was set at 1×10^5 ions with charge exclusion of z = 1 and z > 7. The MS/MS spectra were acquired at a resolution of 15000 (at *m/z* 400). Isolation window was set at 1.6 Th. Dynamic exclusion was employed within 30 s. Data are available via ProteomeXchange with identifier PXD041197.

Data Processing

Data were searched using MaxQuant (version 1.6.6.0) [1,2] using the Andromeda search engine [3] against a reference proteome of Mus musculus (53449 entries, downloaded from Uniprot the $24^{th\ of}$ July 2018). A modified sequence of the protein MTP18 with a Flag tag in its N-ter part was also searched.

bioRxiv preprint doi: https://doi.org/10.1101/2023.04.26.538374; this version posted April 28, 2023. The copyright holder for this preprint (which was not certified by peer review) is the author/funder, who has granted bioRxiv a license to display the preprint in perpetuity. It is made available under aCC-BY 4.0 International license.

The following search parameters were applied: carbamidomethylation of cysteines was set as a fixed modification, oxidation of methionine and protein N-terminal acetylation were set as variable modifications. The mass tolerances in MS and MS/MS were set to 5 ppm and 20 ppm respectively. Maximum peptide charge was set to 7 and 5 amino acids were required as minimum peptide length. A false discovery rate of 1% was set up for both protein and peptide levels. The iBAQ intensity was used to estimate the protein abundance within a sample.

Quantitative analysis was based on pairwise comparison of intensities. Values were log-transformed (log2). Reverse hits and potential contaminant were removed from the analysis. Proteins with at least 2 peptides (including one unique peptide) were kept for further statistics. Intensities values were normalized by median centering within conditions (normalizeD function of the R package DAPAR). Remaining proteins without any iBAQ value in one of both conditions have been considered as proteins quantitatively present in a condition and absent in the other. They have therefore been set aside and considered as differentially abundant proteins. Next, missing values were imputed using the impute.MLE function of the R package imp4. Statistical testing was conducted using a limma t-test thanks to the R package limma[113]. An adaptive Benjamini-Hochberg procedure was applied on the resulting p-values thanks to the function adjust.p of R package cp4p[114] using the robust method previously described[115] to estimate the proportion of true null hypotheses among the set of statistical tests. The proteins associated to an adjusted p-value inferior to a FDR level of 1% have been considered as significantly differentially abundant proteins. Mass spectrometry data have been deposited at the ProteomeXchange Consortium (http://www.proteomexchange.org) via the PRIDE partner repository[103,104] with dataset identifier that is pending

Liver RNA sequencing and RT-qPCR

Total RNA was isolated from 50–100 mg of snap-frozen liver tissue by the NucleoSpin RNA kit (Macherey-Nagel, 740955). Quality control was performed on an Agilent BioAnalyzer. Libraries were built using a TruSeq Stranded mRNA library Preparation Kit (Illumina, USA) following the manufacturer's protocol. Two runs of RNA sequencing were performed for each library on an Illumina NextSeq 500 platform using paired-end 75bp. The RNA-seq analysis was performed with

bioRxiv preprint doi: https://doi.org/10.1101/2023.04.26.538374; this version posted April 28, 2023. The copyright holder for this preprint (which was not certified by peer review) is the author/funder, who has granted bioRxiv a license to display the preprint in perpetuity. It is made available under aCC-BY 4.0 International license.

Sequana. In particular, we used the RNA-seq pipeline (version 0.9.13) (https://github.com/sequana/sequana_rnaseq) built on top of Snakemake 5.8.1[78]. Reads were trimmed from adapters using Cutadapt 2.10 then mapped to the mouse reference genome GRCm38 using STAR 2.7.3a[79]. FeatureCounts 2.0.0 was used to produce the count matrix, assigning reads to features using annotation from Ensembl GRCm38_92 with strand-specificity information[80]. Quality control statistics were summarized using MultiQC 1.8[81]. Statistical analysis on the count matrix was performed to identify differentially regulated genes, comparing different diets among same genotypes or different genotypes under same diet. Clustering of transcriptomic profiles were assessed using a Principal Component Analysis (PCA). Differential expression testing was conducted using DESeq2 library 1.24.0[82] scripts based on SARTools 1.7.0 indicating the significance (Benjamini-Hochberg adjusted p-values, false discovery rate FDR < 0.05) and the effect size (fold-change) for each comparison. Over-representation analysis (ORA) was performed to determine if genes modulated by HFD in control or LMKO mice are more present in specific pathways. ORA was performed on WebGestalt (https://www.webgestalt.org/). RNAseq data have been deposited at ENA with the dataset identifier E-MTAB-12920.

For RT-qPCR, 1 µg of total RNA was converted into cDNA using the iScript Reverse Transcription Supermix (Bio-Rad). RT-qPCR was performed using the CFX384 Touch Real-Time PCR Detection System (Bio-Rad) and SYBR® Green Master Mix (Bio-Rad) using the primers listed in Supplemental Dataset 4. Gapdh was amplified as internal standard. Data were analyzed according to the 2−ΔΔCT method[83].

Primary hepatocyte isolation and imaging

Primary hepatocytes were isolated from 6-8 week-old mice as previously described[84]. Briefly, a catheter (22G feeding needle) was connected to a pump and inserted into the vena cava. Livers were perfused first with perfusion buffer (NaCl 0.15M; Potassium Chloride (KCl, 2.7mM; EuroMedex; P017); Sodium phosphate dibasic (Na_2HPO_4, 0.2mM; Sigma-Aldrich 255793); HEPES-KOH pH 7.4 10mM and EDTA 0.5mM, pH 7.65) at the speed of 3.5 ml/min for 10 minutes, and then with the collagenase buffer (NaCl 0.15M, KCl 2.7mM, Na_2HPO_4 0.2mM, HEPES-KOH pH 7.4 10mM, Calcium Chloride ($CaCl_2$, 0.8mM; Sigma-Aldrich C3881) and Collagenase type I

bioRxiv preprint doi: https://doi.org/10.1101/2023.04.26.538374; this version posted April 28, 2023. The copyright holder for this preprint (which was not certified by peer review) is the author/funder, who has granted bioRxiv a license to display the preprint in perpetuity. It is made available under aCC-BY 4.0 International license.

500µg/ml (Thermo Fisher Scientific, 17018029). Liver lobes were collected in Washing Medium (William's medium (Thermo Fisher Scientific) supplemented with 10% Fetal Bovine Serum (FBS; GIBCO, 10270), a mix of penicillin (100U/ml) and streptomycin (100µg/ml) (Pen-Strep; Sigma-Aldrich, P4333) and amphotericin B (Fungizone, 250ng/ml; GIBCO, 15290018)) and passed through a cell strainer. Cells were centrifuged at 40g for 2 minutes, supernatant was removed and resuspended again with Washing Medium. This procedure was repeated 3 times. Finally, hepatocytes were counted with Trypan Blue using the Countless II FL Automated Cell counter (Invitrogen) and plated at 1.2×10^5 cells/cm^2 in Culturing Medium (William's medium supplemented with 20% FBS, a mix of Insulin (1,7µM), Transferrin (68,75nM) and Selenium (38,73nM) (ITS; Sigma-Aldrich, I3146), dexamethasone (25nM; Sigma-Aldrich, D4902), penicillin (100U/ml) and streptomycin (100µg/ml) and Fungizone (250ng/ml) on pre-coated plates (collagen I (40µg/ml, Gibco) and glacial acetic acid 0.1% (Sigma-Aldrich, A6283); and incubated at 37°C then washed with PBS.

For cell death assays, primary hepatocytes were seeded in Cell Carrier Ultra 96-well plates (PerkinElmer, 6055302), treated with NucBlue Solution (Thermo Fisher)) (diluted 1 drop in 10 ml) for 30 minutes, then, after 2 washes in PBS, cells were treated or not with hydrogen peroxide (H_2O_2, 1mM; Sigma-Aldrich, 95294) in the presence of Propidium Iodide (PI; Thermo Fisher, 640922) (1:500).. Cells were immediately imaged with the Operetta CLS High-Content imaging system (PerkinElmer) at 37°C and 5% CO_2. Images were taken every 2 hours for 10 hours with a 20x water-immersion objective (1.0 NA). PI and NucBlue were excited with the 530-560nm and 355-385nm LEDs respectively. Images were analyzed using Harmony 4.9 software (Perkin Elmer) using the analysis sequence in Supplemental Dataset 4.

Quantification of mitochondrial morphology: primary hepatocytes were isolated from mitoYFP+ mice and seeded in Cell Carrier Ultra 96-well plates, treated with 2µM NucBlue for 30 minutes, then, after 2 washes in PBS. Cells were immediately imaged with the Operetta CLS High Content imaging system at 37°C and 5% CO_2. Images were taken 16 hours post-plating with a 63x water-immersion objective (1.15 NA). MitoYFP and Hoechst were excited with the 460-490nm and 355-385nm LEDs respectively. Images were analyzed using the PhenoLOGIC supervised machine learning pipeline in Harmony 4.9 software (Perkin Elmer) with the analysis sequence in Table 4.

bioRxiv preprint doi: https://doi.org/10.1101/2023.04.26.538374; this version posted April 28, 2023. The copyright holder for this preprint (which was not certified by peer review) is the author/funder, who has granted bioRxiv a license to display the preprint in perpetuity. It is made available under aCC-BY 4.0 International license.

The algorithm was used to identify the best properties able to segregate into “Short” or “Long” populations according to their mitochondrial network. 50 cells of each population were manually selected to for supervised machine learning training. Dead cells identified by propidium iodide were excluded directly by the algorithm and not included in the quantification. To mimic HFD steatosis in primary hepatocytes isolated, culture medium of the cells was supplemented with Intralipid (0.65%) for 24 hours. Intralipid is a complex lipid emulsion composed linoleic, oleic, palmitic, and stearic acids. BODIPY™ 558/568 C12 (Invitrogen D3835) was used to stain intracellular lipid accumulation.

Statistical Analyses

Experiments were repeated at least three times and quantitative analyses were conducted blindly. Randomization of groups (e.g., different genotypes) was performed when simultaneous, parallel measurements were not performed (e.g., Oroboros, hepatocyte isolation). For high-throughput measurements (e.g., mitochondrial morphology, cell death), all groups were measured in parallel to reduce experimental bias. Statistical analyses were performed using GraphPad Prism v9 software. Data are presented as mean ± SD or SEM where indicated. The statistical tests used, and value of experiment replicates are described in the figure legends. Comparisons between two groups were performed by unpaired two-tailed T test. To compare more than two groups or groups at multiple time points 1-way ANOVA or 2-way ANOVA was applied. Tests were considered significant at p-value < 0.05 (*p< 0.05; **p< 0.01; ***p < 0.001; ****p< 0.0001).

bioRxiv preprint doi: https://doi.org/10.1101/2023.04.26.538374; this version posted April 28, 2023. The copyright holder for this preprint (which was not certified by peer review) is the author/funder, who has granted bioRxiv a license to display the preprint in perpetuity. It is made available under aCC-BY 4.0 International license.

Figure legends

Figure 1. Hepatic deletion of *Mtfp1* in mice does not impair basal liver function.

A) Generation of hepatocyte-specific *Mtfp1* knockout mice (LMKO). Conditional $Mtfp1^{LoxP/LoxP}$ mice were crossed to Alb-Cre recombinase mice to generate LMKO mice. *Mtfp1* exons 2 and 3 are flanked by LoxP sites (blue arrowheads) and a single FRT site (green arrowhead), which are excised by Cre-recombinase to yield the deleted (Δ) *Mtfp1* allele.

B) PCR genotyping of Mtfp1 alleles from DNA isolated from indicated different organs of a control and a LMKO mice allele-specific primers (Supplemental Dataset 4).

C) Normalized *Mtfp1* expression in liver in control and LMKO mice at 24-weeks measured by RNAseq (Supplemental Dataset 1). n=4. Data are means ± SD, unpaired Student's t test.****p<0.001.

D) MTFP1, VDAC1, TOMM40 and TIMM20 protein levels. Equal amounts of protein extracted from livers of control (n=4) and LMKO (n=4) mice at 8 weeks of age separated by SDS-PAGE and immunoblotted with indicated antibodies.

E) Genotype distribution from $Mtfp1^{LoxP/LoxP}$ $Alb\text{-}Cre^{tg/+}$ x $Mtfp1^{LoxP/LoxP}$ intercrosses were not different from expected Mendelian distributions using two-tailed binomial tests of live female (n=202; p>0.9999) and male (n=155; p=0.7481) mice.

F) (Top) Representative images of livers from control and LMKO mice fed at 24 weeks of age. Scale bar=1cm. (Bottom) Representative H&E staining n=4-5. Scale bar=100μm.

G) Liver mass of 24-week old control and LMKO mice fed a normal chow (NCD) n=9. Data are means ± SD. unpaired Student's t test, ns=not significant

H) Alanine (ALAT; left) and Aspartate transaminase (ASAT; right) levels in plasma of control (n=3) and LMKO (n=3) mice. Data are means ± SD. unpaired Student's t test, ns=not significant . *: p<0.05.

I) Cholesterol (left) and triglycerides (TG, right) levels in plasma from G). Data are means ± SD. unpaired Student's t test, ns=not significant.

J) Metabolic cage analyses of NCD-fed control and LMKO mice at 24 weeks of age. Total distance covered, food, and water during dark and light phases n=3. Data are means ± SD. unpaired Student's t test, **: p<0.01. ns=not significant

bioRxiv preprint doi: https://doi.org/10.1101/2023.04.26.538374; this version posted April 28, 2023. The copyright holder for this preprint (which was not certified by peer review) is the author/funder, who has granted bioRxiv a license to display the preprint in perpetuity. It is made available under aCC-BY 4.0 International license.

Figure 2. *Mtfp1* deletion promotes mitochondrial respiration via OXPHOS upregulation

A) Substrates from fatty acid oxidation (mustard) and glycolysis (purple, blue) are metabolized in the TCA cycle which delivers fuels the electron transport chain (ETC) complexes by providing NADH and FADH to complexes I (purple) and II (blue), respectively. ETC creates an electrochemical gradient driving the phosphorylation of ADP by Complex V. Specific inhibitors of complex I (rotenone), complex V (oligomycin).

B) Oxygen flux (JO_2) of isolated liver mitochondria from 16-week old control and LMKO mice on NCD measured in the presence of pyruvate, glutamate, and malate (state 2) or succinate and rotenone (state 2) or palmitoyl carnitine and malate (state 2) followed by ADP (state 3). Non-phosphorylating respiration was measured in the presence of oligomycin (state 4). Respiratory Control Ratio (State3:4) data are represented as the means ± SD of 4 independent experiments. 2-tailed, unpaired Student's t test. *: $p<0.05$.

C) Respiratory Control Ratio (RCR) from 16 week old control and LMKO mice on NCD measured in the presence of pyruvate, glutamate and malate plus ADP (state 3) or palmitoyl carnitine and malate plus ADP(state 3) divided Non-phosphorylating respiration in the presence of oligomycin (state 4).

D) Mitochondrial membrane potential ($\Delta\Psi$) measured by quenching of Rhodamine 123 (RH123) fluorescence in liver mitochondria from B). $\Delta\Psi$ was measured in presence of pyruvate, malate, and glutamate (PGM) (state 2) followed by the addition of ADP (state 3) and Oligomycin (OLGM, state 4), CCCP and potassium cyanide (KCN). Data represent mean ± SD; Multiple t-test.

E) Complex IV activity assessed in isolated liver mitochondria from NCD-fed 16-week old control and LMKO mice by recording oxygen flux (JO_2) in the presence of Antimycin A (AMA), Ascorbate and N,N,N′,N′-Tetramethyl-p-phenylenediamine dihydrochloride (TMPD), previously incubated with of pyruvate, glutamate, and malate (PGM) and ADP. n=5. Data are means ± SD. 2-tailed, unpaired Student's t test. *: $p<0.05$.

F) Complex V (ATP synthase) activity assessed in isolated liver mitochondria from NCD-fed 16-week old control and LMKO mice in the reverse mode in the presence of ATP. Oligomycin

bioRxiv preprint doi: https://doi.org/10.1101/2023.04.26.538374; this version posted April 28, 2023. The copyright holder for this preprint (which was not certified by peer review) is the author/funder, who has granted bioRxiv a license to display the preprint in perpetuity. It is made available under aCC-BY 4.0 International license.

(OLGM) or ADP were used as negative controls. n=10. Data are means ± SD. 2-tailed, unpaired Student's t test. *: p<0.05.

G) Mitoplast respiration assessment. Mitoplasts were supplied with either NADH, malate, and ADP (complex I) or FADH, rotenone, and ADP (complex II) n=5. Data are means ± SD. 2-tailed, unpaired Student's t test. *: p<0.05.

H) (Top) Volcano plot of liver proteome of LMKO mice analyzed by mass spectrometry.(Purple) Mitochondrial proteins (MitoCarta 3.0), (Green) Non-mitochondrial proteins more abundant in control liver. (Blue) Non-mitochondrial proteins significantly more abundant in LMKO liver. (Bottom) Relative complex abundance (RCA) plot comparing the levels of the OXPHOS complexes (CI-CV) and the mitoribosome (mtribo) between LMKO and control mice fed. NCD. The graph represents the relative values of each complex ratio between LMKO and controls. The dotted line represents the control mean value of each complex and error bars represent 95% confidence interval of the mean. Paired t-test. *** = p<0.001, ns=non-significant.

I) Proteins levels of different OXPHOS complexes subunits. Equal amounts of protein extracted from hepatic mitochondria isolated from NCD-fed 16-week old control (n=4) and LMKO (n=4) mice were separated by SDS-PAGE, immunoblotted with indicated antibodies (left) and quantified by densitometry (right) relative to Timm22 loading control. Data are means ± SD. 2-tailed, unpaired Student's t test. *: p<0.05.

J) 1D BN-PAGE (left) and densitometric quantification (right) of OXPHOS complexes in hepatic mitochondria isolated from NCD-fed 16-weeks old control and LMKO. n=4. Data are means ± SD. 2-tailed, unpaired Student's t test. *: p<0.05.

Figure 3. MTFP1 interacts with various IMM components in the liver.

A) Generation of transgenic (Tg) Hepatocyte$^{FLAG\text{-}MTFP1}$ mice constitutively expressing FLAG-MTFP1 from the *Ros26* locus.

B) Protease protection assay of liver mitochondria isolated from control and transgenic (Tg) Hepatocyte$^{FLAG\text{-}MTFP1}$ mice analyzed by immunoblot with indicated antibodies.

C) Liver mitochondria co-immunoprecipitation (co-IP) in WT and FALG_MTFP1 mitochondria. Elution fraction (Elu).

bioRxiv preprint doi: https://doi.org/10.1101/2023.04.26.538374; this version posted April 28, 2023. The copyright holder for this preprint (which was not certified by peer review) is the author/funder, who has granted bioRxiv a license to display the preprint in perpetuity. It is made available under aCC-BY 4.0 International license.

D) Volcano plot of the FLAG-MTFP1 interactome analyzed by mass spectrometry (left). (Purple) Mitochondrial proteins exclusively present in FLAG-MTFP1 eluates (binary interactors) or enriched greater than two-fold listed in Supplementary Data 5. (Green) Non-mitochondrial proteins enriched in Hepatocyte$^{FLAG\text{-}MTFP1}$ livers. (Blue) Non-mitochondrial proteins enriched in control liver. (Right) Functional classification of 113 mitochondrial proteins identified in Co-IP eluates (Supplementary Data 4).

E) Second dimension electrophoresis (2D BN-PAGE) analysis of hepatic mitochondria isolated from control (top) and cMKO (bottom) mice fed a NCD immunoblotted using the indicated antibodies.

Figure 4. Hepatic deletion of *Mtfp1* protects mice from high fat diet-induced steatosis.

A) Representative images of livers from control and LMKO mice fed a normal chow diet (NCD, from Fig. 1D) or a high fat diet (HFD) for 16 weeks.

B) Liver weight of 24-week old control and LMKO mice fed a NCD or HFD for 16 weeks. n=7. Data are means ± SD. 2-way ANOVA, *: p<0.05, **: p<0.01, ***: p<0.001, ****: p<0.0001

C) Body mass of control and LMKO mice fed a NCD or HFD for16 weeks. n=7. Data are means ± SD. 2-way ANOVA, *: p<0.05, **: p<0.01, ***: p<0.001, ****: p<0.0001.

D) Triglycerides (TG) measurement in liver tissue from 24-week old control and LMKO mice fed a NCD or HFD for 16 weeks. n=4-5. Data are means ± SD. 2-way ANOVA, **: p<0.01,

E) H&E staining of control and LMKO livers from A). Scale bar=100μm.

F) Alanine (ALAT; left) and Aspartate transaminase (ASAT; right) levels in plasma of 24-week old control and LMKO mice fed a NCD or HFD for 16 weeks. Data are means ± SD. 2-way ANOVA, *: p<0.05, ***: p<0.001, ****: p<0.0001

G) Differential modulation of liver gene expression by HFD. Upregulation (left) and downregulation (right) of mitochondrial (pink) and non-mitochondrial genes (orange or teal) in LMKO and control livers.

H) Pathway enrichment analysis of differentially expressed genes depicted in G).

I) TUNEL staining of control and LMKO livers from A). Scale bar=100μm

bioRxiv preprint doi: https://doi.org/10.1101/2023.04.26.538374; this version posted April 28, 2023. The copyright holder for this preprint (which was not certified by peer review) is the author/funder, who has granted bioRxiv a license to display the preprint in perpetuity. It is made available under aCC-BY 4.0 International license.

Figure 5. LMKO mice are protected against diet-induced metabolic dysregulation

A) Whole-body Respiratory Exchange ratios (RER; VCO_2/VO_2) in control and LMKO mice after 16 weeks of HFD. n=3. Data are means ± SD. 2-way ANOVA, **: p<0.01.

B) Pyruvate Tolerance Test performed after 18h fasting. Left panel: glycaemia measured at indicated time. Right panel: area under the curve (AUC). n=4 NCD; n=5 HFD groups. Data are means ± SD. 2-way ANOVA, *: p<0.05, **: p<0.01, ****: p<0.0001.

C) Glucose Tolerance Test performed after 18h fasting. Left panel: glycaemia measured at indicated time. Right panel: area under the curve (AUC). n=4-9. Data are means ± SD 2-way ANOVA, **: p<0.01.

D) Insulin Tolerance Test performed after 6 hours fasting. Left panel: glycaemia measured at indicated time after insulin injection. Right panel: area under the curve (AUC). n=4. Data are means ± SD. 2-way ANOVA, *: p<0.05, **: p<0.01, ***: p<0.0001, ****: p<0.0001.

E) Body composition analysis of control and LMKO mice fed NCD or HFD by Nuclear Magnetic Resonance (NMR). n=5. Left panel: fat mass; right panel: lean mass. Data are means ± SD. 2-way ANOVA, *: p<0.05, **: p<0.01, ***: p<0.0001, ns=not significant

F) Plasma cholesterol (left) and triglycerides (TG) in control and LMKO mice fed NCD or HFD. n=4-5. Data are means ± SD. 2-way ANOVA, *: p<0.05, **: p<0.01, ***: p<0.0001, ns=not significant

G) Epididymal white adipose tissue (eWAT) mass in control and LMKO mice fed NCD or HFD. n=5 NCD, n=7 HFD. Data are means ± SD. 2-way ANOVA, *: p<0.05, **: p<0.01.

H) Ex vivo steatosis measurement. Representative images of primary hepatocytes isolated from control and LMKO mice treated with IntraLipid (0.65%) for 24h and stained for nuclei (NucBlue, blue) and lipid droplets (BODIPY, orange).

I) BODIPY intensity quantification of H) Data are means of 3 independent experiments ± SD. unpaired Student's t test, **: p<0.01

Figure 6. Hepatic deletion of *Mtfp1* protects mice from FAS-induced liver damage.

A) Representative images of livers from control (n=2) and LMKO (n=4) mice treated with FAS or NaCl for 24 hours.

bioRxiv preprint doi: https://doi.org/10.1101/2023.04.26.538374; this version posted April 28, 2023. The copyright holder for this preprint (which was not certified by peer review) is the author/funder, who has granted bioRxiv a license to display the preprint in perpetuity. It is made available under aCC-BY 4.0 International license.

B) Alanine (ALAT; left) and Aspartate transaminase (ASAT; right) levels in plasma of mice from A). Data are means ± SD. unpaired Student's t test, *: p<0.05, **: p<0.01.

C) H&E staining of control and LMKO livers from A). Scale bar=100μm.

D) TUNEL staining of control and LMKO livers from A). Scale bar=100μm.

E) Representative of high content imaging of primary hepatocytes from control and LMKO mice treated with or without H_2O_2 at 4 hours (1mM) treatment. Blue: nuclei; Orange: propidium iodide (PI).

F) Cell death quantification of PI uptake of 3 independent experiments from E). Data are means ± SEM. 2-way ANOVA, *: p<0.05.

G) Mitochondrial permeability transition pore (mPTP) opening assay. Liver mitochondria from control and LMKO mice were treated with $CaCl_2$ 120μM to induce the mPTP opening by light scattering at 540nm. Cyclosporin A (CsA) 1 μM used to block mPTP opening. Data are means of 3 independent experiments ± SEM. 2-way ANOVA, *: p<0.05.

Figure 7. Model for the regulation of liver resilience by MTFP1

Mtfp1 deletion in hepatocytes of liver-specific Mtfp1 knockout (LMKO) mice promotes liver resilience in vivo by 1) increasing the resistance to mitochondrial permeability transition pore (mPTP) opening and liver apoptosis and 2) enhancing oxidative phosphorylation (OXPHOS) activity and resistance against fatty liver disease (hepatic steatosis) induced by chronic high fat diet (HFD) feeding.

Supplemental Figures

Figure S1. Generation and characterization of *Mtfp1* hepatocyte-specific knockout mice

A) Targeting strategy for conditional inactivation of mouse *Mtfp1* in LMKO mice. To allow deletion of *Mtfp1* exons 2 and 3 were flanked in both cases by LoxP sites (blue arrowheads). Flox denotes NeoR cassette containing LoxP targeted locus. LoxP denotes NeoR cassette-deleted targeted locus. Δ denotes deletion induced by Cre-recombinase. FRT sites (green) initially flank NeoR cassette (yellow). Exons 2 and 3 were deleted by Cre-recombinase.

B) Genotyping PCR for the distal LoxP site in the conditional *Mftp1* locus from genomic DNA.

bioRxiv preprint doi: https://doi.org/10.1101/2023.04.26.538374; this version posted April 28, 2023. The copyright holder for this preprint (which was not certified by peer review) is the author/funder, who has granted bioRxiv a license to display the preprint in perpetuity. It is made available under aCC-BY 4.0 International license.

The wild type (WT; 387 bp) and the conditional (LoxP; 469 bp) alleles are shown for *Mtfp*$^{WT/WT}$, *Mtfp1*$^{LoxP/WT}$, and *Mtfp1*$^{LoxP/LoxP}$ mice.

C) Respiratory Exchange Ratio (RER) for control and LMKO mice on fed a normal chow diet (NCD). RER analyses for 24 hours are shown. Mean values for day and night periods. N=4. Data are means ± SD. 2-tailed, unpaired Student's t test. ns=not significant.

D) Upregulated (orange) and downregulated (cyan) genes in LMKO mice on a normal chow diet corresponding to Supplemental Dataset 1.

Figure S2. Impact of *Mtfp1* deletion on mitochondrial mass

A) Representative images of primary hepatocytes isolated from control and LMKO mice expressing mitoYFP (green). Nuclei in blue. Scale bar=100μm.

B) Quantification of mitochondrial imaging in primary hepatocytes from control and LMKO expressing mitoYFP mice. Single cell mitoYFP intensity is normalized to hepatocyte area.

C) Quantification of mitochondrial morphology in primary hepatocytes from control and LMKO mice performed by supervised machine learning.

D) Mitochondrial DNA content measured by qPCR relative to nuclear DNA in liver biopsies from control and LMKO mice fed a normal chow (NCD) or high-fat (HFD) diets for 16 weeks. N=4. Data are means ± SD. 2-way ANOVA, *: $p<0.05$. **: $p<0.01$.

E) Mitochondrial surface determined by transmission electron microscopy (TEM) of control and LMKO liver sections. Median (yellow dotted line) and Quartiles (solid colored line). 2-tailed, unpaired Student's t test. ns=not significant.

Figure S3. Diet-induced transcriptional remodeling in control and LMKO mice

A) Venn diagram overlap of upregulated genes in LMKO and control mice on normal chow diet (NCD) or high fat diet (HFD) corresponding to Supplemental Dataset 1.

A) Venn diagram overlap of downregulated genes in LMKO and control mice on normal chow diet (NCD) or high fat diet (HFD) corresponding to Supplemental Dataset 1.

Figure S4. Diet-induced proteomic remodeling in control and LMKO mice

bioRxiv preprint doi: https://doi.org/10.1101/2023.04.26.538374; this version posted April 28, 2023. The copyright holder for this preprint (which was not certified by peer review) is the author/funder, who has granted bioRxiv a license to display the preprint in perpetuity. It is made available under aCC-BY 4.0 International license.

A) (Top) Volcano plot of liver proteome of LMKO mice analyzed by mass spectrometry.(Purple) Mitochondrial proteins (MitoCarta 3.0), (Green) Enriched non-mitochondrial proteins more (Blue) Enriched non-mitochondrial proteins corresponding to Supplemental Dataset 3.
B) Relative complex abundance (RCA) plot comparing the levels of the OXPHOS complexes (CI-CV) and the mitoribosome (mtribo). The graph represents the relative values of each complex ratio between two groups. The dotted line represents the control mean value of each complex and error bars represent 95% confidence interval of the mean. Paired t-test. *** = p<0.001, ns= non-significant.

Figure S5. LMKO mice are protected against diet-induced metabolic dysregulation
A) Total food consumption during dark and light phases in HFD-fed control and LMKO mice. n=3. Data are means ± SD. unpaired Student's t test, ns=not significant.
B) Total water consumption during dark and light phases in HFD-fed control and LMKO mice n.=3. Data are means ± SD. unpaired Student's t test, ns=not significant.
C) Total distance covered during dark and light phases in HFD-fed control and LMKO mice. n=3. Data are means ± SD. unpaired Student's t test, ns=not significant
D) Plasma insulin levels measured in control and LMKO mice treated fed with NCD or HFD after 16 hours fasting (0 minute) or fasting followed by glucose injection (30 minutes). n=4-5. Data are means ± SD. 2-way ANOVA, ***: p<0.001
E) Representative images of extrahepatic white adipose tissue (eWAT) after H&E staining from control and LMKO mice fed with NCD or HFD for 16 weeks. n=4-5. Scale bar=100μm.
F) Quantification of adipocyte area in G).Data are means ± SD. 2-way ANOVA, *: p<0.05.
G) Body weight of control and LMKO mice on NCD and HFD. Data are means ± SD
H) Fasting glycaemia of control and LMKO mice on NCD and HFD. Data are means ± SD

Figure S6. Hepatic deletion of *Mtfp1* protects mice from FAS-induced liver damage.
A) Lactate dehydrogenase (LDH) plasma levels of 16-week old control and LMKO after treatment with FAS (n=4) or NaCl (n=2) for 24 hours. Data are means ± SD. 2-tailed, unpaired Student's t test. *: p<0.05

bioRxiv preprint doi: https://doi.org/10.1101/2023.04.26.538374; this version posted April 28, 2023. The copyright holder for this preprint (which was not certified by peer review) is the author/funder, who has granted bioRxiv a license to display the preprint in perpetuity. It is made available under aCC-BY 4.0 International license.

B) Liver to body weight ratio of 16-week old control and LMKO before and after treatment with FAS (n=6) or NaCl (n=4) for 24 hours. Data are means ± SD. 2-way ANOVA, *: p<0.05 ns=not significant.

Figure S7. Differential MTFP1 expression in animal models and human patients

A) Venn diagram comparison of differentially expressed genes in MTFP1-deficient livers and hearts from LMKO and cMKO mice. LMKO data are reported in Supplemental Dataset 1 and cMKO data were reported previously[15].

B) Venn diagram comparison of differentially expressed proteins in MTFP1-deficient livers and hearts from LMKO and cMKO mice. LMKO data are reported in Supplemental Dataset 2 and cMKO data were reported previously[15].

C) Violin plot of *MTFP1* expression (transcripts per kilobase (TPkB) in NASH human patients biopsies (GSE162694) previously analyzed[67]. F0-F4 scale refers to the severity of the severity of fibrosis as previously described[85]. Data are means ± SD. 1-way ANOVA, **: p<0.01 ****: p<0.0001.

bioRxiv preprint doi: https://doi.org/10.1101/2023.04.26.538374; this version posted April 28, 2023. The copyright holder for this preprint (which was not certified by peer review) is the author/funder, who has granted bioRxiv a license to display the preprint in perpetuity. It is made available under aCC-BY 4.0 International license.

References

1. Samuel, V. T. & Shulman, G. I. Nonalcoholic Fatty Liver Disease as a Nexus of Metabolic and Hepatic Diseases. *Cell Metab.* **27**, 22–41 (2018).
2. Ye, Q. *et al.* Global prevalence, incidence, and outcomes of non-obese or lean non-alcoholic fatty liver disease: a systematic review and meta-analysis. *Lancet Gastroenterol Hepatol* **5**, 739–752 (2020).
3. Tilg, H. & Moschen, A. R. Evolution of inflammation in nonalcoholic fatty liver disease: the multiple parallel hits hypothesis. *Hepatology* **52**, 1836–1846 (2010).
4. Fromenty, B. & Roden, M. Mitochondrial alterations in fatty liver diseases. *J. Hepatol.* **78**, 415–429 (2023).
5. Giacomello, M., Pyakurel, A., Glytsou, C. & Scorrano, L. The cell biology of mitochondrial membrane dynamics. *Nat. Rev. Mol. Cell Biol.* **21**, 204–224 (2020).
6. Riley, J. S. & Tait, S. W. Mitochondrial DNA in inflammation and immunity. *EMBO Rep.* **21**, e49799 (2020).
7. Nassir, F. & Ibdah, J. A. Role of mitochondria in nonalcoholic fatty liver disease. *Int. J. Mol. Sci.* **15**, 8713–8742 (2014).
8. García-Ruiz, I. *et al.* High-fat diet decreases activity of the oxidative phosphorylation complexes and causes nonalcoholic steatohepatitis in mice. *Dis. Model. Mech.* **7**, 1287–1296 (2014).
9. Gorman, G. S. *et al.* Mitochondrial diseases. *Nat Rev Dis Primers* **2**, 16080 (2016).
10. Koliaki, C. *et al.* Adaptation of hepatic mitochondrial function in humans with non-alcoholic fatty liver is lost in steatohepatitis. *Cell Metab.* **21**, 739–746 (2015).
11. Sanyal, A. J. *et al.* Nonalcoholic steatohepatitis: Association of insulin resistance and mitochondrial abnormalities. *Gastroenterology* **120**, 1183–1192 (2001).
12. Perry, R. J., Zhang, D., Zhang, X.-M., Boyer, J. L. & Shulman, G. I. Controlled-release mitochondrial protonophore reverses diabetes and steatohepatitis in rats. *Science* **347**, 1253–1256 (2015).

bioRxiv preprint doi: https://doi.org/10.1101/2023.04.26.538374; this version posted April 28, 2023. The copyright holder for this preprint (which was not certified by peer review) is the author/funder, who has granted bioRxiv a license to display the preprint in perpetuity. It is made available under aCC-BY 4.0 International license.

13. Goedeke, L. *et al.* Controlled-release mitochondrial protonophore (CRMP) reverses dyslipidemia and hepatic steatosis in dysmetabolic nonhuman primates. *Sci. Transl. Med.* **11**, (2019).
14. Parascandola, J. Dinitrophenol and bioenergetics: an historical perspective. *Mol. Cell. Biochem.* **5**, 69–77 (1974).
15. Donnarumma, E. *et al.* Mitochondrial Fission Process 1 controls inner membrane integrity and protects against heart failure. *Nat. Commun.* **13**, 6634 (2022).
16. Tondera, D. The mitochondrial protein MTP18 contributes to mitochondrial fission in mammalian cells. *J Cell Sci* **118**, 3049–3059 (2005).
17. Morita, M. *et al.* mTOR Controls Mitochondrial Dynamics and Cell Survival via MTFP1. *Mol. Cell* **67**, 922-935.e5 (2017).
18. Zhang, Y. *et al.* MTP18 overexpression contributes to tumor growth and metastasis and associates with poor survival in hepatocellular carcinoma. *Cell Death Dis.* **9**, 956 (2018).
19. Tondera, D. *et al.* Knockdown of MTP18, a novel phosphatidylinositol 3-kinase-dependent protein, affects mitochondrial morphology and induces apoptosis. *J. Biol. Chem.* **279**, 31544–31555 (2004).
20. Duroux-Richard, I. *et al.* miR-125b controls monocyte adaptation to inflammation through mitochondrial metabolism and dynamics. *Blood* **128**, 3125–3136 (2016).
21. Ryaboshapkina, M. & Hammar, M. Human hepatic gene expression signature of non-alcoholic fatty liver disease progression, a meta-analysis. *Sci. Rep.* **7**, 12361 (2017).
22. Donnarumma, E. *et al.* Mitochondrial fission process 1 (MTFP1) controls bioenergetic efficiency and prevents inflammatory cardiomyopathy and heart failure in mice. *bioRxiv* 2021.10.21.465262 (2021) doi:10.1101/2021.10.21.465262.
23. Cretin, E. *et al.* High-throughput screening identifies suppressors of mitochondrial fragmentation in OPA1 fibroblasts. *EMBO Mol. Med.* **13**, e13579 (2021).
24. Rath, S. *et al.* MitoCarta3.0: an updated mitochondrial proteome now with sub-organelle localization and pathway annotations. *Nucleic Acids Res.* **49**, D1541–D1547 (2021).
25. Soltis, A. R. *et al.* Hepatic Dysfunction Caused by Consumption of a High-Fat Diet. *Cell Rep.* **21**, 3317–3328 (2017).

bioRxiv preprint doi: https://doi.org/10.1101/2023.04.26.538374; this version posted April 28, 2023. The copyright holder for this preprint (which was not certified by peer review) is the author/funder, who has granted bioRxiv a license to display the preprint in perpetuity. It is made available under aCC-BY 4.0 International license.

1171 26. Commerford, S. R. *et al.* Diets enriched in sucrose or fat increase gluconeogenesis and G-6-
1172 Pase but not basal glucose production in rats. *American Journal of Physiology-Endocrinology*
1173 *and Metabolism* **283**, E545–E555 (2002).
1174 27. Lemonnier, D. Effect of age, sex, and site on the cellularity of the adipose tissue in mice and
1175 rats rendered obese by a high-fat diet. *J Clin Invest* **51**, 2907–2915 (1972).
1176 28. Aung, L. H. H., Li, R., Prabhakar, B. S., Maker, A. V. & Li, P. Mitochondrial protein 18 (MTP18)
1177 plays a pro-apoptotic role in chemotherapy-induced gastric cancer cell apoptosis. *Oncotarget*
1178 **8**, 56582–56597 (2017).
1179 29. Varanita, T. *et al.* The OPA1-dependent mitochondrial cristae remodeling pathway controls
1180 atrophic, apoptotic, and ischemic tissue damage. *Cell Metab.* **21**, 834–844 (2015).
1181 30. Elmore, S. A. *et al.* Recommendations from the INHAND Apoptosis/Necrosis Working Group.
1182 *Toxicol Pathol* **44**, 173–188 (2016).
1183 31. Baines, C. P. *et al.* Loss of cyclophilin D reveals a critical role for mitochondrial permeability
1184 transition in cell death. *Nature* **434**, 658–662 (2005).
1185 32. Karch, J. *et al.* Inhibition of mitochondrial permeability transition by deletion of the ANT family
1186 and CypD. *Sci Adv* **5**, eaaw4597 (2019).
1187 33. Sebastián, D. *et al.* Mitofusin 2 (Mfn2) links mitochondrial and endoplasmic reticulum function
1188 with insulin signaling and is essential for normal glucose homeostasis. *Proc. Natl. Acad. Sci.*
1189 *U. S. A.* **109**, 5523–5528 (2012).
1190 34. Huang, Q. *et al.* TFAM loss induces nuclear actin assembly upon mDia2 malonylation to
1191 promote liver cancer metastasis. *EMBO J.* **41**, e110324 (2022).
1192 35. Yamada, T. *et al.* Prevention and regression of megamitochondria and steatosis by blocking
1193 mitochondrial fusion in the liver. *iScience* **25**, 103996 (2022).
1194 36. Cho, J. *et al.* Mitochondrial ATP transporter depletion protects mice against liver steatosis and
1195 insulin resistance. *Nat. Commun.* **8**, 14477 (2017).
1196 37. Lesner, N. P. *et al.* Differential requirements for mitochondrial electron transport chain
1197 components in the adult murine liver. *Elife* **11**, (2022).
1198 38. Aung, L. H. H. *et al.* Mitochondrial protein 18 is a positive apoptotic regulator in
1199 cardiomyocytes under oxidative stress. *Clin. Sci.* **133**, 1067–1084 (2019).

bioRxiv preprint doi: https://doi.org/10.1101/2023.04.26.538374; this version posted April 28, 2023. The copyright holder for this preprint (which was not certified by peer review) is the author/funder, who has granted bioRxiv a license to display the preprint in perpetuity. It is made available under aCC-BY 4.0 International license.

39. Yakar, S. *et al.* Normal growth and development in the absence of hepatic insulin-like growth factor I. *PNAS* **96**, 7324–7329 (1999).

40. Hill, B. G. *et al.* Integration of cellular bioenergetics with mitochondrial quality control and autophagy. *Biol. Chem.* **393**, 1485–1512 (2012).

41. Moyes, C. D., Mathieu-Costello, O. A., Brill, R. W. & Hochachka, P. W. Mitochondrial metabolism of cardiac and skeletal muscles from a fast (Katsuwonus pelamis) and a slow (Cyprinus carpio) fish. *Can. J. Zool.* **70**, 1246–1253 (1992).

42. Suarez, R. K. Oxygen and the upper limits to animal design and performance. *J. Exp. Biol.* **201**, 1065–1072 (1998).

43. Srere, P. A. Organization of proteins within the mitochondrion. *Organized multienzyme systems. Catalytic properties* 1–61 (1985).

44. Forner, F., Foster, L. J., Campanaro, S., Valle, G. & Mann, M. Quantitative proteomic comparison of rat mitochondria from muscle, heart, and liver. *Mol. Cell. Proteomics* **5**, 608–619 (2006).

45. Kim, T.-Y. *et al.* Metabolic labeling reveals proteome dynamics of mouse mitochondria. *Mol. Cell. Proteomics* **11**, 1586–1594 (2012).

46. Gross, N. J. Control of mitochondrial turnover under the influence of thyroid hormone. *J. Cell Biol.* **48**, 29–40 (1971).

47. Jakovcic, S., Swift, H. H., Gross, N. J. & Rabinowitz, M. Biochemical and stereological analysis of rat liver mitochondria in different thyroid states. *J. Cell Biol.* **77**, 887–901 (1978).

48. Arruda, A. P. *et al.* Chronic enrichment of hepatic endoplasmic reticulum-mitochondria contact leads to mitochondrial dysfunction in obesity. *Nat. Med.* **20**, 1427–1435 (2014).

49. Chouchani, E. T. *et al.* Complex I deficiency due to selective loss of Ndufs4 in the mouse heart results in severe hypertrophic cardiomyopathy. *PLoS One* **9**, e94157 (2014).

50. Wai, T. *et al.* Imbalanced OPA1 processing and mitochondrial fragmentation cause heart failure in mice. *Science* **350**, aad0116 (2015).

51. Piquereau, J. *et al.* Down-regulation of OPA1 alters mouse mitochondrial morphology, PTP function, and cardiac adaptation to pressure overload. *Cardiovasc. Res.* **94**, 408–417 (2012).

bioRxiv preprint doi: https://doi.org/10.1101/2023.04.26.538374; this version posted April 28, 2023. The copyright holder for this preprint (which was not certified by peer review) is the author/funder, who has granted bioRxiv a license to display the preprint in perpetuity. It is made available under aCC-BY 4.0 International license.

52. Song, M., Mihara, K., Chen, Y., Scorrano, L. & Dorn, G. W., 2nd. Mitochondrial fission and fusion factors reciprocally orchestrate mitophagic culling in mouse hearts and cultured fibroblasts. *Cell Metab.* **21**, 273–286 (2015).
53. Graham, B. H. *et al.* A mouse model for mitochondrial myopathy and cardiomyopathy resulting from a deficiency in the heart/muscle isoform of the adenine nucleotide translocator. *Nat. Genet.* **16**, 226–234 (1997).
54. Anderson, C. J. *et al.* ALS/FTD mutant CHCHD10 mice reveal a tissue-specific toxic gain-of-function and mitochondrial stress response. *Acta Neuropathol.* **138**, 103–121 (2019).
55. Genin, E. C. *et al.* Mitochondrial defect in muscle precedes neuromuscular junction degeneration and motor neuron death in CHCHD10S59L/+ mouse. *Acta Neuropathol.* **138**, 123–145 (2019).
56. Ashrafian, H. *et al.* A mutation in the mitochondrial fission gene Dnm1l leads to cardiomyopathy. *PLoS Genet.* **6**, e1001000 (2010).
57. Agnew, T. *et al.* A Wars2 mutant mouse model displays OXPHOS deficiencies and activation of tissue-specific stress response pathways. *Cell Rep.* **25**, 3315-3328.e6 (2018).
58. Fan, W. *et al.* A mouse model of mitochondrial disease reveals germline selection against severe mtDNA mutations. *Science* **319**, 958–962 (2008).
59. Vafai, S. B. & Mootha, V. K. Mitochondrial disorders as windows into an ancient organelle. *Nature* **491**, 374–383 (2012).
60. Molinié, T. *et al.* MDH2 produced OAA is a metabolic switch rewiring the fuelling of respiratory chain and TCA cycle. *Biochim. Biophys. Acta Bioenerg.* **1863**, 148532 (2022).
61. Benard, G. *et al.* Physiological diversity of mitochondrial oxidative phosphorylation. *Am. J. Physiol. Cell Physiol.* **291**, C1172-82 (2006).
62. Beutner, G., Alanzalon, R. E. & Porter, G. A., Jr. Cyclophilin D regulates the dynamic assembly of mitochondrial ATP synthase into synthasomes. *Sci. Rep.* **7**, 14488 (2017).
63. Carraro, M. *et al.* The Unique Cysteine of F-ATP Synthase OSCP Subunit Participates in Modulation of the Permeability Transition Pore. *Cell Rep.* **32**, 108095 (2020).
64. Chinopoulos, C. *et al.* Modulation of F0F1-ATP synthase activity by cyclophilin D regulates matrix adenine nucleotide levels. *FEBS J.* **278**, 1112–1125 (2011).

bioRxiv preprint doi: https://doi.org/10.1101/2023.04.26.538374; this version posted April 28, 2023. The copyright holder for this preprint (which was not certified by peer review) is the author/funder, who has granted bioRxiv a license to display the preprint in perpetuity. It is made available under aCC-BY 4.0 International license.

65. Giorgio, V. *et al.* Cyclophilin D modulates mitochondrial F0F1-ATP synthase by interacting with the lateral stalk of the complex. *J. Biol. Chem.* **284**, 33982–33988 (2009).
66. Lu, Y.-W. *et al.* Human adenine nucleotide translocases physically and functionally interact with respirasomes. *Mol. Biol. Cell* **28**, 1489–1506 (2017).
67. Benegiamo, G. *et al.* The genetic background shapes the susceptibility to mitochondrial dysfunction and NASH progression. *J. Exp. Med.* **220**, (2023).
68. Sterky, F. H., Lee, S., Wibom, R., Olson, L. & Larsson, N.-G. Impaired mitochondrial transport and Parkin-independent degeneration of respiratory chain-deficient dopamine neurons in vivo. *Proc. Natl. Acad. Sci. U. S. A.* **108**, 12937–12942 (2011).
69. Wittig, I., Braun, H.-P. & Schägger, H. Blue native PAGE. *Nat. Protoc.* **1**, 418–428 (2006).
70. Gilda, J. E. & Gomes, A. V. Stain-Free total protein staining is a superior loading control to β-actin for Western blots. *Anal. Biochem.* **440**, 186–188 (2013).
71. Kulak, N. A., Pichler, G., Paron, I., Nagaraj, N. & Mann, M. Minimal, encapsulated proteomic-sample processing applied to copy-number estimation in eukaryotic cells. *Nat Methods* **11**, 319–324 (2014).
72. Rappsilber, J., Mann, M. & Ishihama, Y. Protocol for micro-purification, enrichment, pre-fractionation and storage of peptides for proteomics using StageTips. *Nat Protoc* **2**, 1896–1906 (2007).
73. Tyanova, S., Temu, T. & Cox, J. The MaxQuant computational platform for mass spectrometry-based shotgun proteomics. *Nat Protoc* **11**, 2301–2319 (2016).
74. Schwanhäusser, B. *et al.* Global quantification of mammalian gene expression control. *Nature* **473**, 337–342 (2011).
75. Tyanova, S. *et al.* The Perseus computational platform for comprehensive analysis of (prote)omics data. *Nat. Methods* **13**, 731–740 (2016).
76. Perez-Riverol, Y. *et al.* The PRIDE database and related tools and resources in 2019: improving support for quantification data. *Nucleic Acids Research* **47**, D442–D450 (2019).
77. Vizcaíno, J. A. *et al.* ProteomeXchange provides globally coordinated proteomics data submission and dissemination. *Nat Biotechnol* **32**, 223–226 (2014).

bioRxiv preprint doi: https://doi.org/10.1101/2023.04.26.538374; this version posted April 28, 2023. The copyright holder for this preprint (which was not certified by peer review) is the author/funder, who has granted bioRxiv a license to display the preprint in perpetuity. It is made available under aCC-BY 4.0 International license.

78. Köster, J. & Rahmann, S. Snakemake--a scalable bioinformatics workflow engine. *Bioinformatics* **28**, 2520–2522 (2012).

79. Dobin, A. *et al.* STAR: ultrafast universal RNA-seq aligner. *Bioinformatics* **29**, 15–21 (2013).

80. Liao, Y., Smyth, G. K. & Shi, W. featureCounts: an efficient general purpose program for assigning sequence reads to genomic features. *Bioinformatics* **30**, 923–930 (2014).

81. Ewels, P., Magnusson, M., Lundin, S. & Käller, M. MultiQC: summarize analysis results for multiple tools and samples in a single report. *Bioinformatics* **32**, 3047–3048 (2016).

82. Love, M. I., Huber, W. & Anders, S. Moderated estimation of fold change and dispersion for RNA-seq data with DESeq2. *Genome Biol.* **15**, 550 (2014).

83. Livak, K. J. & Schmittgen, T. D. Analysis of Relative Gene Expression Data Using Real-Time Quantitative PCR and the 2−ΔΔCT Method. *Methods* **25**, 402–408 (2001).

84. Severgnini, M. *et al.* A rapid two-step method for isolation of functional primary mouse hepatocytes: cell characterization and asialoglycoprotein receptor based assay development. *Cytotechnology* **64**, 187–195 (2012).

85. Pantano, L. *et al.* Molecular characterization and cell type composition deconvolution of fibrosis in NAFLD. *Sci. Rep.* **11**, 18045 (2021).

Acknowledgments

We thank David Hardy and Maryse Moya-Nilges for the histology services, Priscilla Lopes and for technical assistance. We thank Nils-Göran Larsson for providing mitoYFP mice, Arnaud Mourier and Marie Lagouge for inciteful discussions, and Marie Lemesle for excellent administrative assistance. T.W. is supported by the European Research Council (ERC) Starting Grant No. 714472 (Acronym "*Mitomorphosis*") and the Agence Nationale pour la Recherche (ANR-20-CE14-0039-02). D.A.S and D.H.H are supported by grants from the Australian National Health and Medical Research Council (GNT2009732) and Medical Research Future Fund (MRF2016030). We acknowledge the Bio21 Mass Spectrometry and Proteomics Facility (MMSPF) for the provision of instrumentation, training, and technical support.

Figure 1

bioRxiv preprint doi: https://doi.org/10.1101/2023.04.26.538374; this version posted April 28, 2023. The copyright holder for this preprint (which was not certified by peer review) is the author/funder, who has granted bioRxiv a license to display the preprint in perpetuity. It is made available under aCC-BY 4.0 International license.

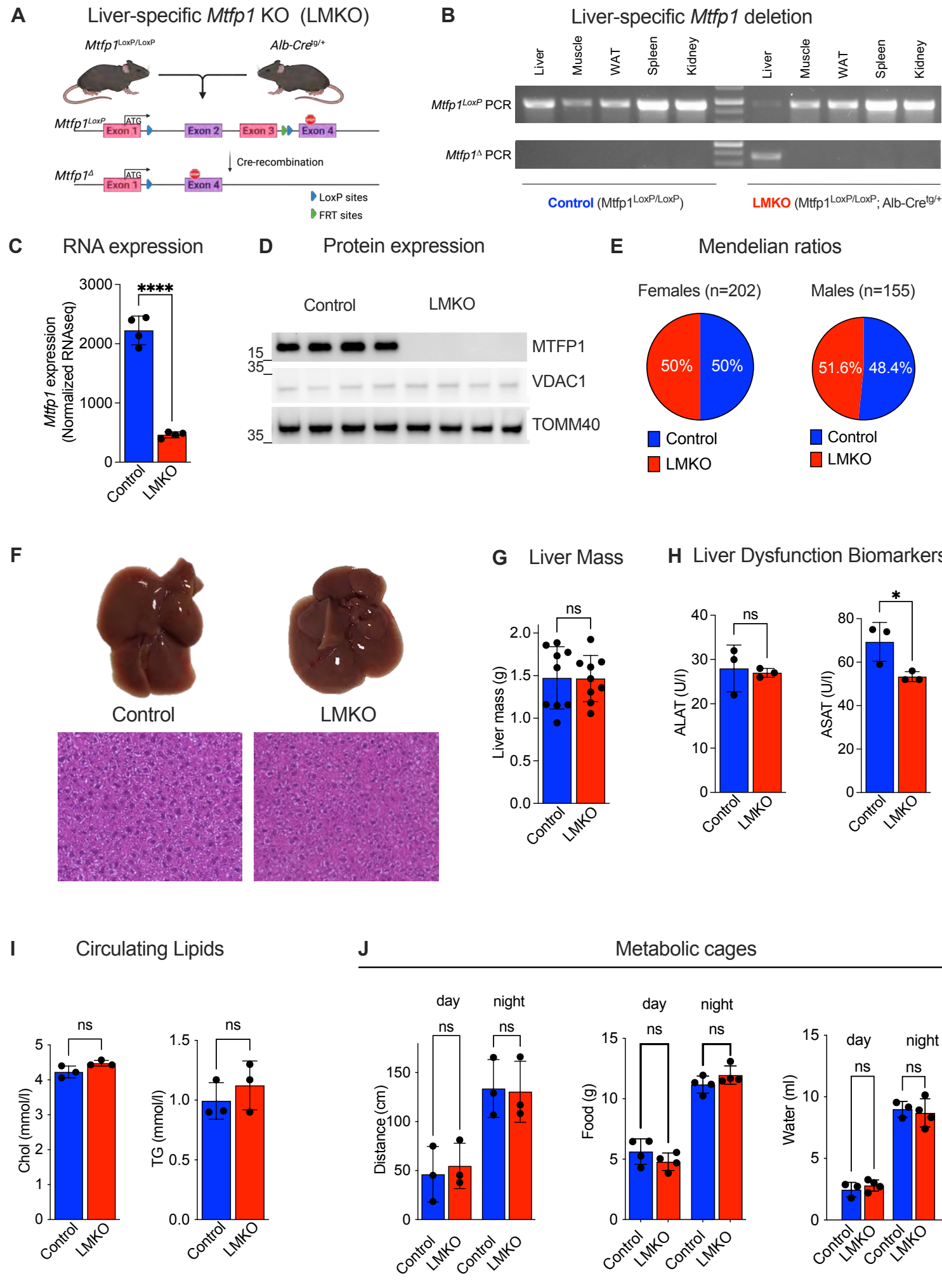
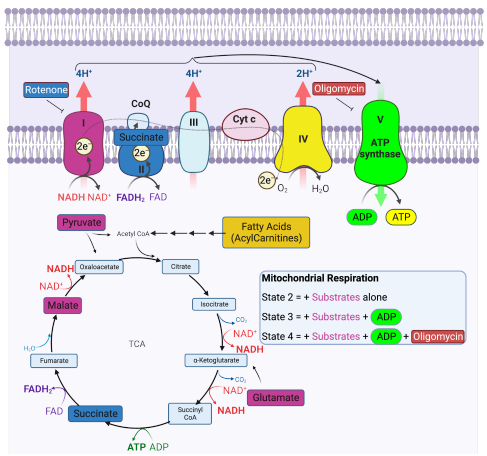
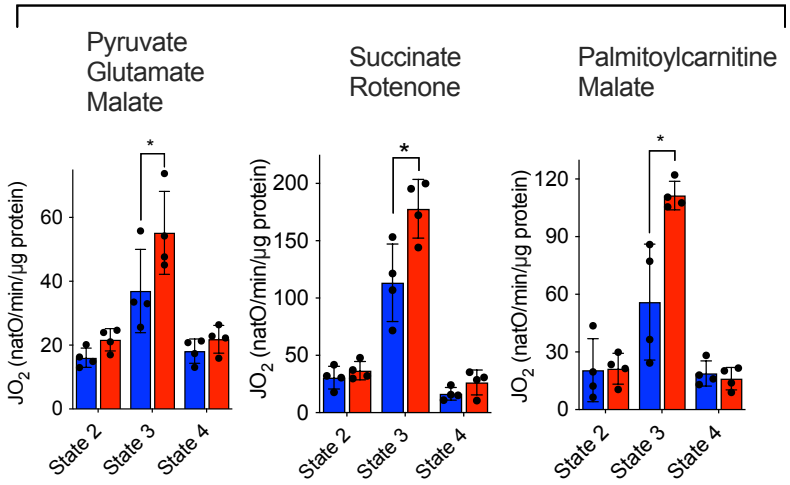
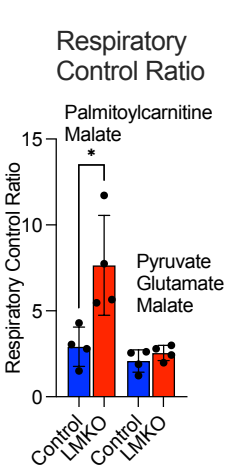
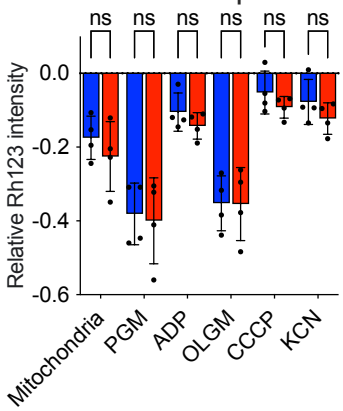


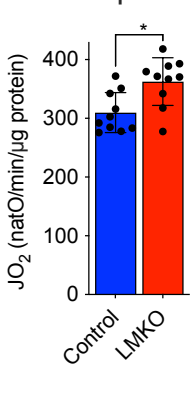
Figure 2

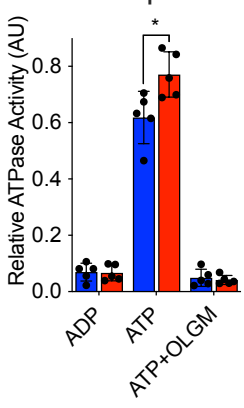

A
Rotenone
Succinate
Cyt c
Oligomycin
ATP synthase
NADH NAD+ FADH2 FAD
Pyruvate
Fatty Acids (AcylCarnitines)
Acetyl CoA
Oxaloacetate
Citrate
Isocitrate
Malate
Fumarate
TCA
α-Ketoglutarate
Succinyl CoA
Glutamate
Succinate
ATP ADP
Mitochondrial Respiration
State 2 = + Substrates alone
State 3 = + Substrates + ADP
State 4 = + Substrates + ADP + Oligomycin

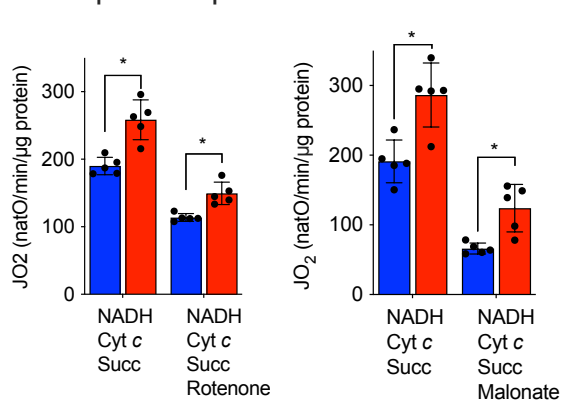

B
Oxygen Consumption
Pyruvate Glutamate Malate
Succinate Rotenone
Palmitoylcarnitine Malate
JO2 (natO/min/µg protein)
State 2
State 3
State 4

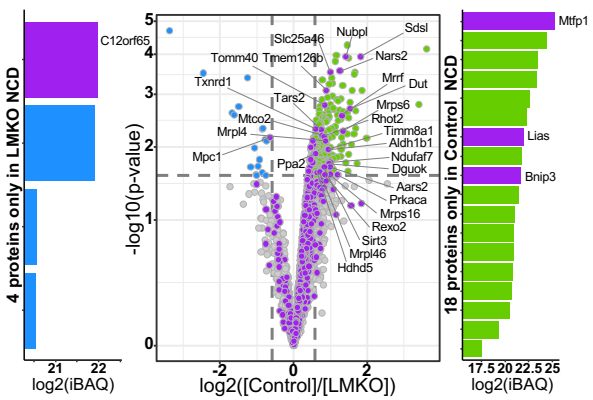

C
Respiratory Control Ratio
Palmitoylcarnitine Malate
Pyruvate Glutamate Malate
Respiratory Control Ratio
Control
LMKO

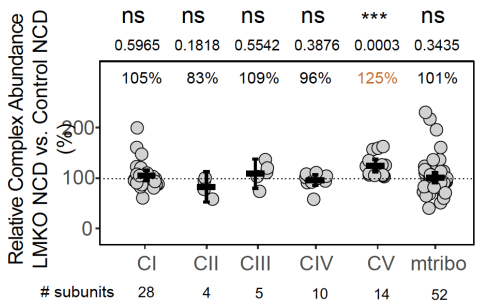

D
Membrane potential
Relative Rh123 intensity
ns
Mitochondria
PGM
ADP
OLGM
CCCP
KCN

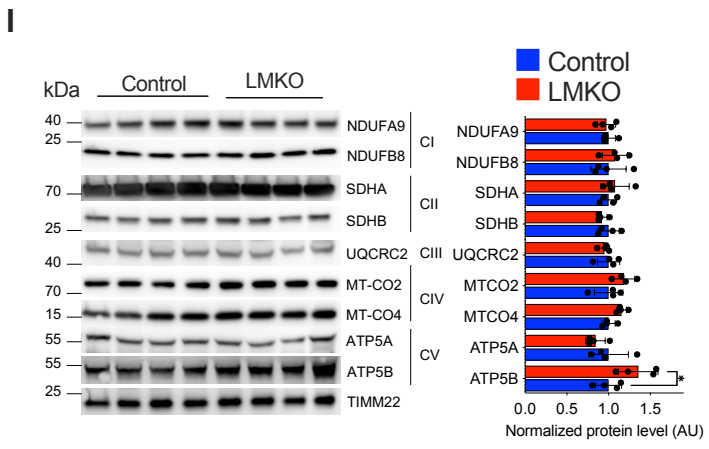

E Complex IV
JO2 (natO/min/µg protein)
Control
LMKO


F Complex V
Relative ATPase Activity (AU)
ADP
ATP
ATP+OLGM


G Mitoplast respiration
JO2 (natO/min/µg protein)
NADH Cyt c Succ
NADH Cyt c Succ Rotenone
NADH Cyt c Succ Malonate


H
Liver proteome
4 proteins only in LMKO NCD
C12orf65
18 proteins only in Control NCD
Mtfp1
Lias
Bnip3
-log10(p-value)
log2([Control]/[LMKO])
log2(iBAQ)


Relative Complex Abundance
Relative Complex Abundance LMKO NCD vs. Control NCD (%)
ns ns ns ns *** ns
0.5965 0.1818 0.5542 0.3876 0.0003 0.3435
105% 83% 109% 96% 125% 101%
CI CII CIII CIV CV mtribo
subunits 28 4 5 10 14 52


I
kDa
Control
LMKO
NDUFA9
NDUFB8
SDHA
SDHB
UQCRC2
MT-CO2
MT-CO4
ATP5A
ATP5B
TIMM22
CI
CII
CIII
CIV
CV
Normalized protein level (AU)

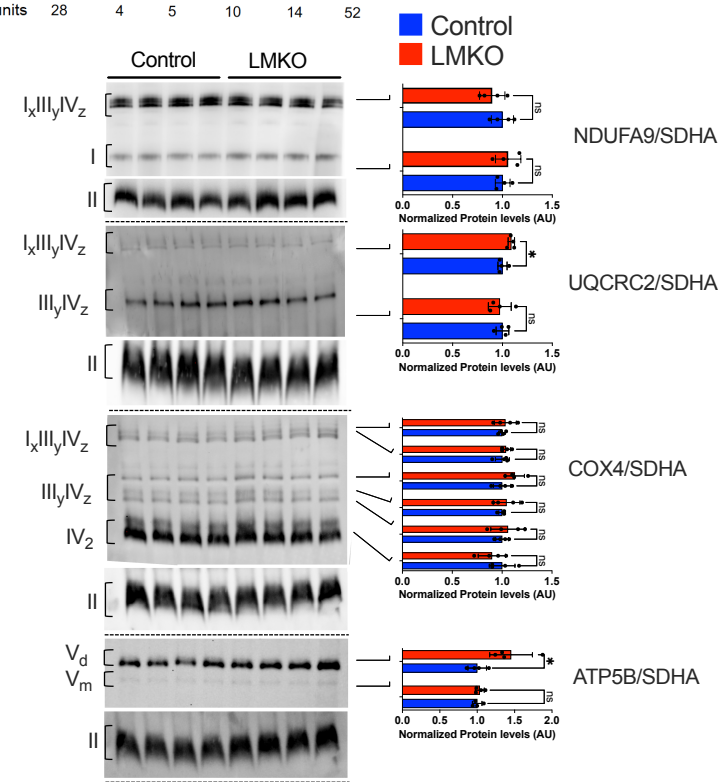

J
Control
LMKO
NDUFA9/SDHA
UQCRC2/SDHA
COX4/SDHA
ATP5B/SDHA
Normalized Protein levels (AU)

FIgure 3

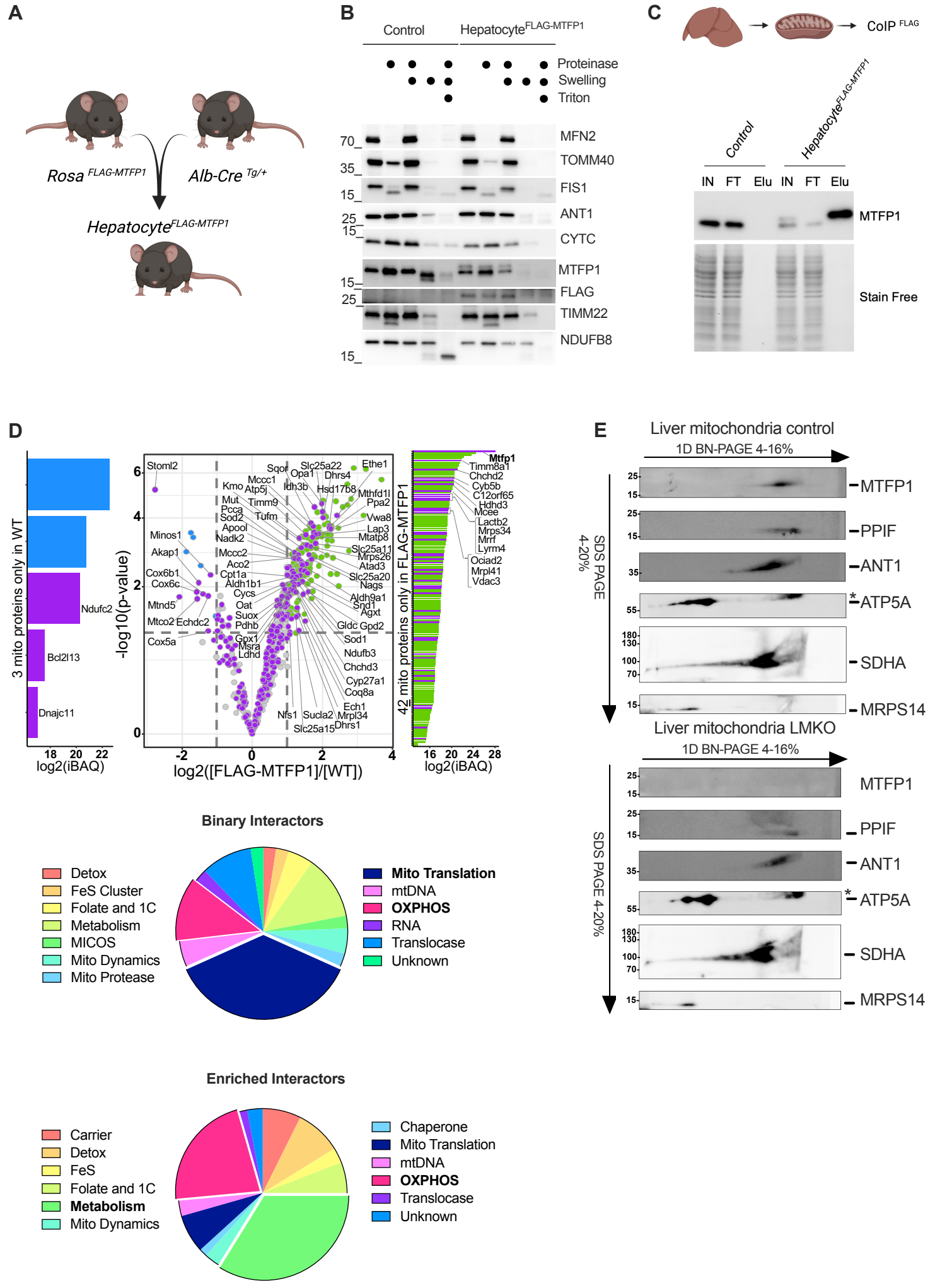

A
Rosa FLAG-MTFP1
Alb-Cre Tg/+
Hepatocyte FLAG-MTFP1
B
Control
Hepatocyte FLAG-MTFP1
Proteinase
Swelling
Triton
70
35
15
25
15
15
25
15
MFN2
TOMM40
FIS1
ANT1
CYTC
MTFP1
FLAG
TIMM22
NDUFB8
C
CoIP FLAG
Control
Hepatocyte FLAG-MTFP1
IN FT Elu IN FT Elu
MTFP1
Stain Free
D
3 mito proteins only in WT
Ndufc2
Bcl2l13
Dnajc11
log2(iBAQ)
-log10(p-value)
log2([FLAG-MTFP1]/[WT])
42 mito proteins only in FLAG-MTFP1
Mtfp1
log2(iBAQ)
Binary Interactors
Detox
FeS Cluster
Folate and 1C
Metabolism
MICOS
Mito Dynamics
Mito Protease
Mito Translation
mtDNA
OXPHOS
RNA
Translocase
Unknown
Enriched Interactors
Carrier
Detox
FeS
Folate and 1C
Metabolism
Mito Dynamics
Chaperone
Mito Translation
mtDNA
OXPHOS
Translocase
Unknown
E
Liver mitochondria control
1D BN-PAGE 4-16%
SDS PAGE 4-20%
MTFP1
PPIF
ANT1
ATP5A
SDHA
MRPS14
Liver mitochondria LMKO
1D BN-PAGE 4-16%
SDS PAGE 4-20%
MTFP1
PPIF
ANT1
ATP5A
SDHA
MRPS14

Figure 4

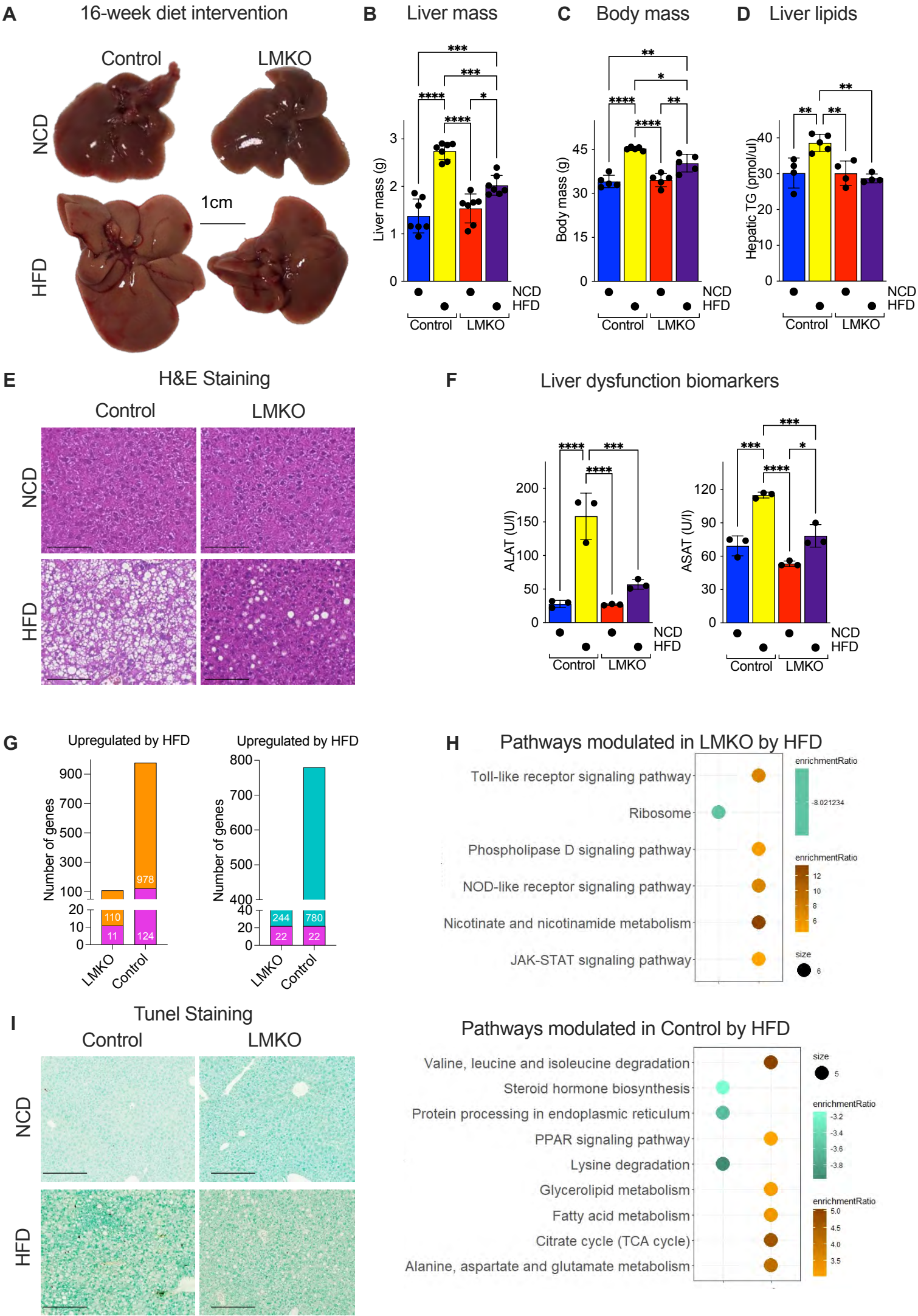

A
16-week diet intervention
Control
LMKO
NCD
HFD
1cm
B
Liver mass
Liver mass (g)
C
Body mass
Body mass (g)
D
Liver lipids
Hepatic TG (pmol/ul)
NCD
HFD
Control
LMKO
E
H&E Staining
F
Liver dysfunction biomarkers
ALAT (U/l)
ASAT (U/l)
G
Upregulated by HFD
Number of genes
978
110
11
124
244
780
22
H
Pathways modulated in LMKO by HFD
Toll-like receptor signaling pathway
Ribosome
Phospholipase D signaling pathway
NOD-like receptor signaling pathway
Nicotinate and nicotinamide metabolism
JAK-STAT signaling pathway
enrichmentRatio
size
I
Tunel Staining
Pathways modulated in Control by HFD
Valine, leucine and isoleucine degradation
Steroid hormone biosynthesis
Protein processing in endoplasmic reticulum
PPAR signaling pathway
Lysine degradation
Glycerolipid metabolism
Fatty acid metabolism
Citrate cycle (TCA cycle)
Alanine, aspartate and glutamate metabolism

Figure 5

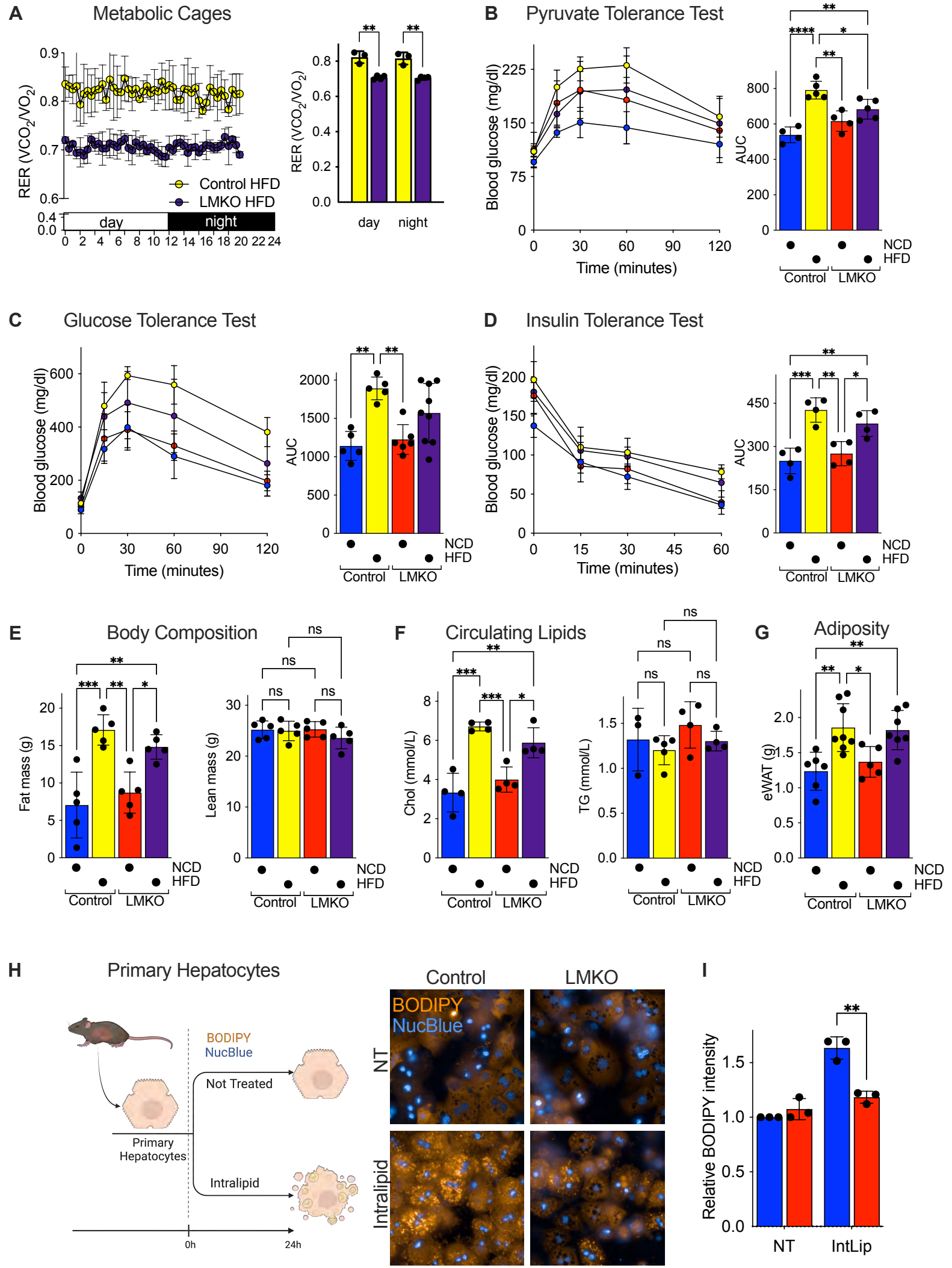

A
Metabolic Cages
RER (VCO2/VO2)
Control HFD
LMKO HFD
day
night
B
Pyruvate Tolerance Test
Blood glucose (mg/dl)
Time (minutes)
AUC
NCD
HFD
Control
LMKO
C
Glucose Tolerance Test
D
Insulin Tolerance Test
E
Body Composition
Fat mass (g)
Lean mass (g)
F
Circulating Lipids
Chol (mmol/L)
TG (mmol/L)
G
Adiposity
eWAT (g)
H
Primary Hepatocytes
BODIPY
NucBlue
Not Treated
Intralipid
0h
24h
NT
I
Relative BODIPY intensity
IntLip

Figure 6

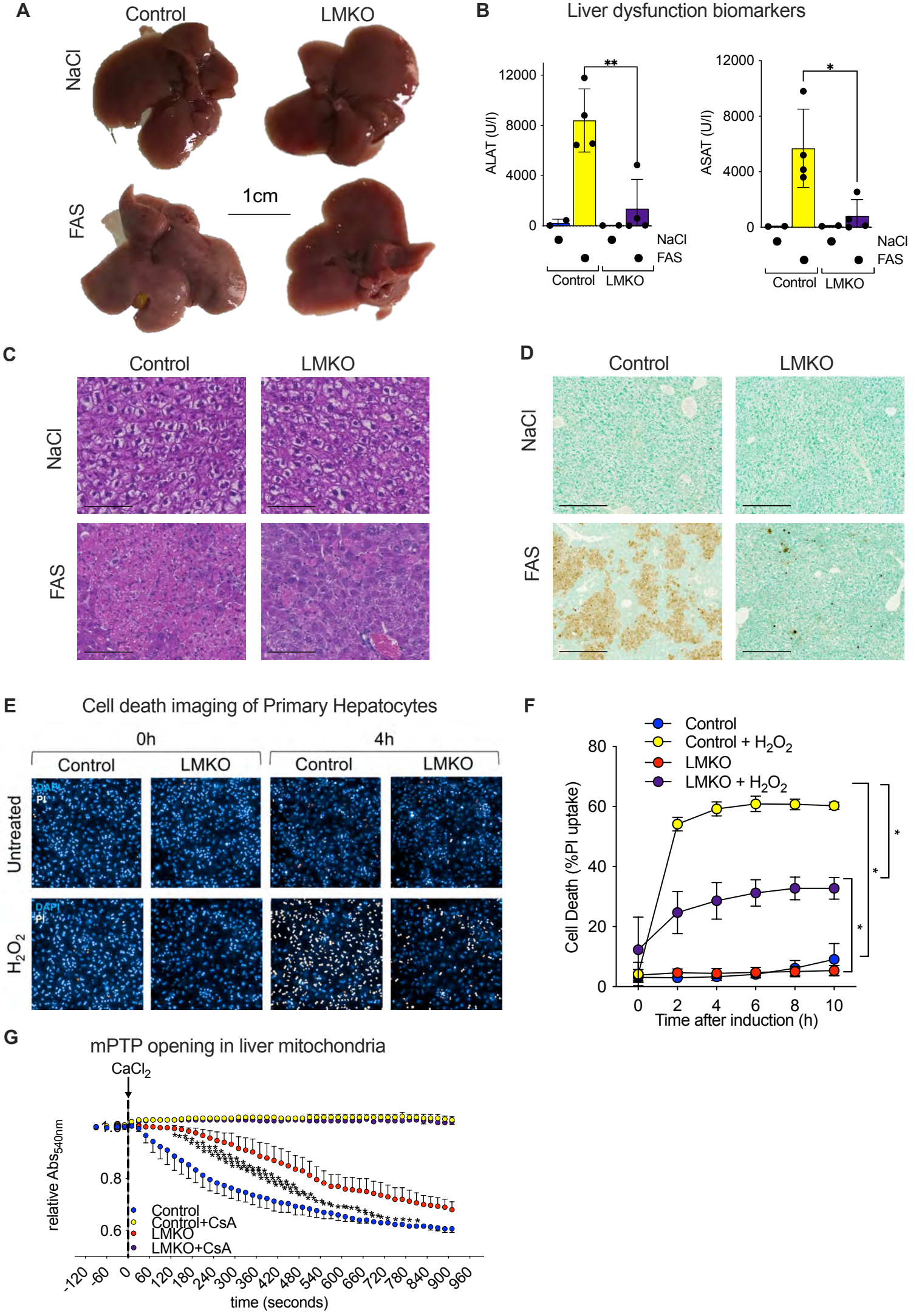
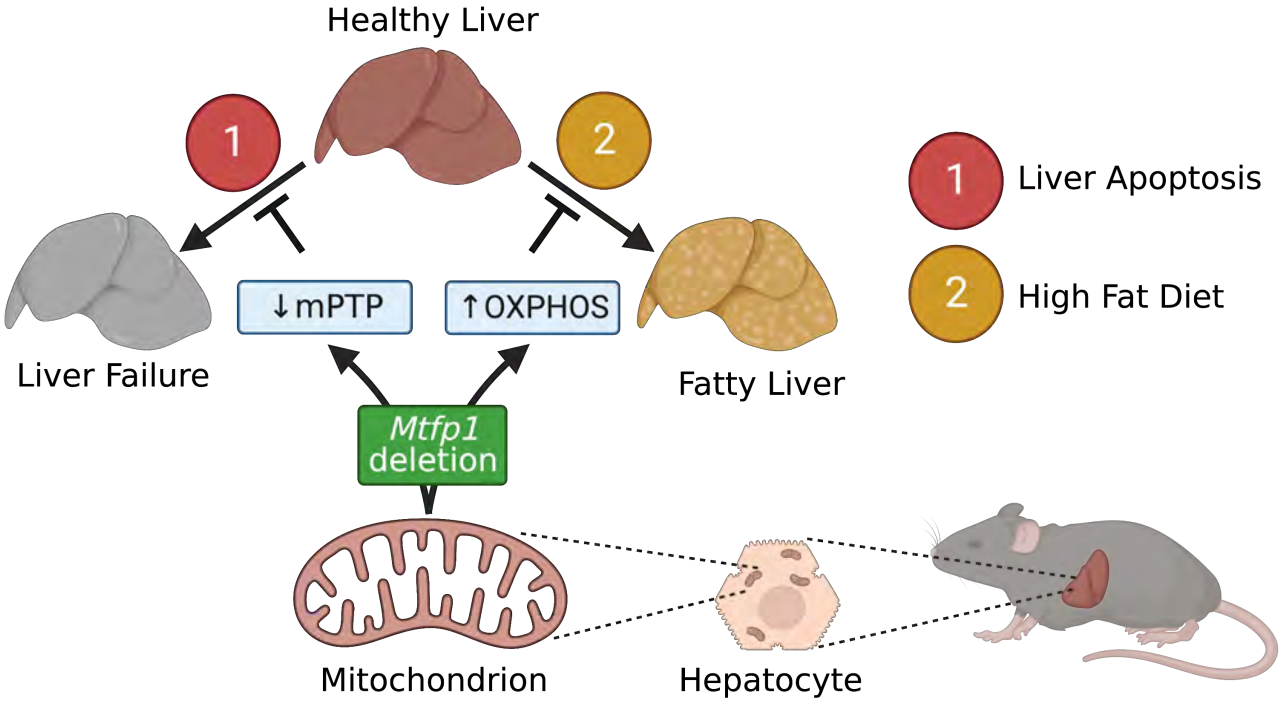

A
Control
LMKO
NaCl
FAS
1cm
B
Liver dysfunction biomarkers
ALAT (U/l)
ASAT (U/l)
12000
8000
4000
0
**
*
NaCl
FAS
Control
LMKO
C
Control
LMKO
NaCl
FAS
D
Control
LMKO
NaCl
FAS
E
Cell death imaging of Primary Hepatocytes
0h
4h
Control
LMKO
Control
LMKO
Untreated
H2O2
DAPI
PI
F
Control
Control + H2O2
LMKO
LMKO + H2O2
Cell Death (%PI uptake)
Time after induction (h)
0
20
40
60
80
0
2
4
6
8
10
*
*
*
G
mPTP opening in liver mitochondria
CaCl2
relative Abs540nm
1.0
0.8
0.6
Control
Control+CsA
LMKO
LMKO+CsA
-120
-60
0
60
120
180
240
300
360
420
480
540
600
660
720
780
840
900
960
time (seconds)

Figure 7


Healthy Liver
1
2
Liver Failure
↓mPTP
↑OXPHOS
Fatty Liver
Mtfp1 deletion
Mitochondrion
Hepatocyte
1 Liver Apoptosis
2 High Fat Diet